

A JET BREAK IN THE X-RAY LIGHT CURVE OF SHORT GRB 111020A: IMPLICATIONS FOR ENERGETICS AND RATES

W. FONG¹, E. BERGER¹, R. MARGUTTI¹, B. A. ZAUDERER¹, E. TROJA², I. CZEKALA¹, R. CHORNOCK¹, N. GEHRELS²,
T. SAKAMOTO², D. B. FOX³, P. PODSIADLOWSKI⁴

Draft version March 3, 2013

ABSTRACT

We present broad-band observations of the afterglow and environment of the short GRB 111020A. An extensive X-ray light curve from *Swift*/XRT, XMM-Newton and *Chandra*, spanning ~ 100 seconds to 10 days after the burst, reveals a significant break at $\delta t \approx 2$ days with pre- and post-break decline rates of $\alpha_{X,1} \approx -0.78$ and $\alpha_{X,2} \lesssim -1.7$, respectively. Interpreted as a jet break, we infer a collimated outflow with an opening angle of $\theta_j \approx 3-8^\circ$. The resulting beaming-corrected γ -ray (10–1000 keV band) and blastwave kinetic energies are $(2-3) \times 10^{48}$ erg and $(0.3-2) \times 10^{49}$ erg, respectively, with the range depending on the unknown redshift of the burst. We report a radio afterglow limit of $< 39 \mu\text{Jy}$ (3σ) from EVLA observations which, along with our finding that $\nu_c < \nu_X$, constrains the circumburst density to $n_0 \sim 0.01-0.1 \text{ cm}^{-3}$. Optical observations provide an afterglow limit of $i \gtrsim 24.4$ mag at 18 hours after the burst, and reveal a potential host galaxy with $i \approx 24.3$ mag. The sub-arcsecond localization from *Chandra* provides a precise offset of $0.80'' \pm 0.11''$ (1σ) from this galaxy corresponding to an offset of 5–7 kpc for $z = 0.5-1.5$. We find a high excess neutral Hydrogen column density of $(7.5 \pm 2.0) \times 10^{21} \text{ cm}^{-2}$ ($z = 0$). Our observations demonstrate that a growing fraction of short GRBs are collimated which may lead to a true event rate of $\gtrsim 100-1000 \text{ Gpc}^{-3} \text{ yr}^{-1}$, in good agreement with the NS-NS merger rate of $\approx 200-3000 \text{ Gpc}^{-3} \text{ yr}^{-1}$. This consistency is promising for coincident short GRB-gravitational wave searches in the forthcoming era of Advanced LIGO/VIRGO.

Subject headings:

1. INTRODUCTION

Observations of the temporal and spectral evolution of short-duration gamma-ray burst (GRB; $T_{90} < 2$ sec; Kouveliotou et al. 1993) afterglows are crucial to our understanding of the basic properties of these events: their energetics, parsec-scale environments, and geometries. From observations over the past 7 years, we now know that short GRBs have isotropic-equivalent energies of $\sim 10^{50}-10^{52}$ erg (Berger 2007) and circumburst densities of $\sim 10^{-6}-1 \text{ cm}^{-3}$ (Soderberg et al. 2006; Panaitescu 2006; Stratta et al. 2007; Perley et al. 2009b; Berger 2010; Fong et al. 2011); however these ranges are based on only a handful of events. The geometry, or degree of collimation, is the least constrained property, but is of particular interest because it directly affects the true energy scale and event rates. These parameters aid our understanding of the explosion physics, the nature of the progenitors, and the potential detectability of short GRBs as gravitational wave sources. In particular, knowledge of the true energy scale may constrain the mechanism of energy extraction from the central engine and the ejecta composition: $\nu\bar{\nu}$ annihilation powering a baryonic jet (Jaroszynski 1993; Mochkovitch et al. 1993) or magnetohydrodynamic (MHD) processes in a magnetically-dominated outflow (Blandford & Znajek 1977; Rosswog et al. 2003). Significant improvement on the short GRB observed rate of $\gtrsim 10 \text{ Gpc}^{-3} \text{ yr}^{-1}$ (Nakar & Granot 2007) will have a critical impact on estimates for coincident short GRB-gravitational wave detections in the era of Advanced LIGO/VIRGO (Abadie et al. 2010).

The opening angles (θ_j) of GRBs can be inferred from temporal breaks in the afterglow light curves (“jet breaks”), which occur at the time, t_j , when the Lorentz factor of the outflow is $\Gamma(t_j) \approx 1/\theta_j$; a later break corresponds to a wider opening angle (Sari et al. 1999; Rhoads 1999). Jet breaks in the light curves of long-duration GRBs have led to an opening angle distribution with a range of $\sim 2-20^\circ$ and a median of 7° , leading to beaming-corrected energies of $E_\gamma = [1 - \cos(\theta_j)]E_{\gamma,\text{iso}} \sim 10^{50}-10^{51}$ erg (Bloom et al. 2003; Frail et al. 2001; Friedman & Bloom 2005; Kocevski & Butler 2008; Racusin et al. 2009). For short GRBs, there is mounting theoretical (Eichler et al. 1989; Narayan et al. 1992) and observational (Fong et al. 2010; Berger 2010; Church et al. 2011) evidence that the progenitors are NS-NS/NS-BH mergers and numerous simulations of post-merger black hole accretion have predicted collimated outflows with $\theta_j \sim 5-20^\circ$ (Popham et al. 1999; Aloy et al. 2005; Rosswog 2005; Rezzolla et al. 2011) up to several tens of degrees (Ruffert & Janka 1999b; Popham et al. 1999; Rezzolla et al. 2011).

However, the detection of jet breaks in the afterglow light curves of short GRBs has proved to be challenging. They can in principle be measured from optical or radio observations, but there are several caveats that make this particularly difficult for short GRBs. First, the brightness of optical and radio afterglows are sensitive to the circumburst densities, which are typically low, $\sim 10^{-2} \text{ cm}^{-3}$ (Soderberg et al. 2006). Indeed, of nearly 70 short bursts detected by *Swift*, only 2 radio afterglows have been detected over the past 7 years (Berger et al. 2005; Soderberg et al. 2006; *Chandra* & Frail 2011). Similarly, only $\sim 30\%$ of *Swift* bursts have detected optical afterglows, with a typical brightness at $\lesssim 1$ day of ≈ 23 mag (Berger 2010; Fong et al. 2011), making long-term temporal monitoring nearly impossible with ground-based facilities. Second, in the optical band there can be significant contamination from the host galaxies, which are generally brighter than the afterglows at $\gtrsim 1$ day (Berger 2010).

¹ Harvard-Smithsonian Center for Astrophysics, 60 Garden Street, Cambridge, MA 02138, USA

² NASA Goddard Space Flight Center, Greenbelt, MD 20771, USA

³ Department of Astronomy and Astrophysics, 525 Davey Laboratory, Pennsylvania State University, University Park, PA 16802, USA

⁴ Department of Astronomy, Oxford University, Oxford, OX1 3RH, UK

On the other hand, the X-ray afterglow brightness is independent of the circumburst density (as long as the density is $\gtrsim 10^{-5} \text{ cm}^{-3}$ and hence $\nu_c > \nu_X$; Granot & Sari 2002), and host contamination is not an issue. In addition, the well-sampled *Swift*/XRT light curves from ~ 1 min to ~ 1 day provide an unambiguous baseline against which we can measure a subsequent break. Therefore, it is no surprise that the X-rays enabled the discovery of the first jet break in a short GRB. The X-ray afterglow light curve of GRB 051221A exhibited a break at ≈ 5 days, leading to $\theta_j \approx 7^\circ$ (Soderberg et al. 2006; Burrows et al. 2006). Similarly, *Chandra* observations of GRB 050724A out to 22 days placed a meaningful lower limit of $\theta_j \gtrsim 25^\circ$ (Grupe et al. 2006), consistent with a spherical explosion. Temporal breaks on timescales of \lesssim few hours were observed in the XRT light curves of GRBs 061201 (Stratta et al. 2007) and 090510⁵ (De Pasquale et al. 2010). If these are interpreted as jet breaks, they would lead to $\theta_j \sim 1^\circ$; however, they also match the timescale and behavior of early breaks in long GRBs, which are not due to collimation (Nousek et al. 2006; Zhang et al. 2006; Liang et al. 2007). Finally, there is tentative evidence for beaming in the light curves of GRBs 050709 (Fox et al. 2005) and 061210⁶ (Berger 2007); however, these are based on sparsely-sampled light curves without a definitive break (e.g., Watson et al. 2006). No other jet breaks in the light curves of unambiguous short GRBs have been reported to date⁷ and the lack of jet breaks in *Swift*/XRT observations out to ~ 1 –2 days can provide only weak lower bounds of $\theta_j \gtrsim 2$ – 6° (revised from Coward et al. 2012 with more realistic density values; see Section 4.2).

Against this backdrop, we present here the discovery of a break in the X-ray light curve of GRB 111020A at $\delta t \approx 2$ days, best explained as a jet break. We also present contemporaneous radio and optical limits on the afterglow, allowing a characterization of the broad-band synchrotron spectrum and constraints on the energy and density. In addition, we report the discovery of a putative host galaxy. A comparison of our X-ray and optical data may require an appreciable amount of extinction and the highest intrinsic neutral Hydrogen column density for a short GRB to date. Our results have strong implications for the opening angle distribution, and therefore the observed short GRB rate and true energy release.

Unless otherwise noted, all magnitudes in this paper are in the AB system and are corrected for Galactic extinction in the direction of the burst using $E(B-V) = 0.432$ mag (Schlegel et al. 1998; Schlafly & Finkbeiner 2011). We employ a standard Λ CDM cosmology with $\Omega_M = 0.27$, $\Omega_\Lambda = 0.73$, and $H_0 = 71 \text{ km s}^{-1} \text{ Mpc}^{-1}$.

2. OBSERVATIONS OF GRB 111020A

2.1. *Swift* Observations

GRB 111020A was detected on 2011 October 20 at 06:33:49.0 UT by the Burst Alert Telescope (BAT) on-board the *Swift* satellite (Gehrels et al. 2004; Sakamoto et al. 2011b). BAT located the burst at a ground-calculated position of RA=19^h08^m06.9^s and Dec=−38°01′50.3″ (J2000) with 2.1′ accuracy (90% containment; Sakamoto et al. 2011a). The

⁵ GRB 090510 also exhibits a post-jet break-like decay in its optical light curve (Nieves Guelbenzu et al. 2012).

⁶ Please note that Berger (2007) erroneously refers to GRB 061006.

⁷ A jet break was reported in the light curve of GRB 090426A (Nieves Guelbenzu et al. 2011); however the characteristics of its environment and prompt emission are more similar to those of long GRBs (Levesque et al. 2010; Xin et al. 2011).

X-ray Telescope (XRT) commenced observations of the location of the burst at $\delta t = 72.8$ s (where δt is the time after the BAT trigger) and detected a fading X-ray source (Section 2.2). The UV-Optical Telescope (UVOT) began observations of the field at $\delta t = 79$ s but no corresponding UV or optical source was found within the XRT position. The 3σ limit in the *white* filter, which transmits over $\lambda = 1600$ – 8000 Å (Poole et al. 2008), is 20.3 mag (not corrected for Galactic extinction; Oates & Sakamoto 2011).

The gamma-ray emission consists of a single pulse with a duration of $T_{90} = 0.40 \pm 0.09$ s in the 15–350 keV band, classifying GRB 111020A as a short burst (Sakamoto et al. 2011a). The spectrum is best fit with a single power law with index 1.37 ± 0.26 and a fluence of $f_\gamma = (6.5 \pm 1.0) \times 10^{-8} \text{ erg cm}^{-2}$ (15–150 keV). Spectral lag analysis is not conclusive, and there is no clear evidence for extended emission (Sakamoto et al. 2011).

2.2. *X-ray* Observations

The XRT promptly located a fading, uncatalogued X-ray source (Evans et al. 2007, 2009; Sakamoto et al. 2011b) with a UVOT-enhanced position of RA=19^h08^m12.53^s and Dec=−38°00′43.8″ (J2000) and an uncertainty of 1.6″ (Osborne et al. 2011). XRT observations of the field continued until the source faded below the detection threshold at $\delta t \approx 3.5$ days.

We also observed the field of GRB 111020A with the European Photon Imaging Camera (EPIC-PN) on-board the X-ray Multi-Mirror Mission (XMM-Newton) starting at $\delta t = 0.65$ days. With 13.5 ks of on-source observations, we clearly detect a source in the energy range 0.5–10 keV, consistent with the *Swift*-XRT position. In addition, we obtained two sets of 20-ks observations with the Advanced CCD Imaging Spectrometer (ACIS-S; 0.3–10 keV) on-board the *Chandra* X-ray Observatory at $\delta t = 2.9$ and 10.1 days to refine the astrometry and monitor the light curve evolution. We detect the X-ray afterglow in the first *Chandra* observation but do not detect any source at the same location in the second epoch.

2.2.1. *Data Analysis and Spectral Fitting*

We analyze the XRT data using the latest version of the HEASOFT package (v.6.11) and relevant calibration files. We apply standard filtering and screening criteria, and generate a count rate light curve following the prescriptions from Margutti et al. (2010) and Margutti et al. (2012). Our re-binning scheme ensures a minimum signal-to-noise ratio of $S/N = 4$ for each temporal bin. We analyze the XMM data using standard routines in the Scientific Analysis System (SAS) v.11. We remove the first 5 ks of data due to high background contamination, giving a total exposure time of 13.5 ks. We extract count rates from a 20″ radius aperture and the background is calculated using 20″ radius source-free regions on the same chip. We use the CIAO data reduction package for the *Chandra* data. For the first epoch, we use a 2.5″ radius source aperture centered on the *Chandra* position and a background annulus with inner and outer radii of 10″ and 35″, respectively, giving a source detection significance of $\sim 30\sigma$. For the second epoch, we extract 1 count in a 2.5″ aperture at the location of the source, consistent with the average background level calculated from source-free regions on the same chip. We therefore take the 3σ background count rate as an upper limit on the X-ray afterglow.

To extract a spectrum from the X-ray data, we fit each of the data sets with an absorbed power law model (*tbabs* ×

tbabs \times *pow* within the XSPEC routine) characterized by a photon index, Γ , and intrinsic neutral hydrogen absorption column, $N_{\text{H,int}}$, in excess of the Galactic column density in the direction of the burst, $N_{\text{H,MW}} = 6.9 \times 10^{20} \text{ cm}^{-2}$ (typical uncertainty of $\sim 10\%$; Kalberla et al. 2005; Wakker et al. 2011), using Cash statistics. For XRT, we utilize data in the time interval 0.08–60 ks where there is no evidence for spectral evolution. We find an average best-fitting (C-stat $_{\nu}$ = 0.86 for 188 d.o.f.) spectrum characterized by $\Gamma = 2.2 \pm 0.5$ and $N_{\text{H,int}} = (1.0 \pm 0.3) \times 10^{22} \text{ cm}^{-2}$ at $z=0$ (Table 1). Uncertainties correspond to the 90% confidence level. Our best-fit parameters are fully consistent with the automatic spectrum fit produced by Mangano & Sakamoto (2011). The XMM data are best modeled with a power law characterized by $\Gamma = 2.0 \pm 0.4$ and $N_{\text{H,int}} = (0.65 \pm 0.22) \times 10^{22} \text{ cm}^{-2}$ (C-stat $_{\nu}$ = 1.0 for 256 d.o.f.), consistent with the XRT model parameters. We also fit the first epoch of *Chandra* data and the resulting parameters are consistent with those from XRT and XMM, albeit with large error bars due to low count statistics (Table 1). Since we find no evidence for spectral evolution in the XRT data, we perform a joint XRT+XMM spectral analysis to obtain the best constraints on Γ and $N_{\text{H,int}}$. The resulting best-fit model has $\Gamma = 2.0 \pm 0.3$ and $N_{\text{H,int}} = (0.8 \pm 0.2) \times 10^{22} \text{ cm}^{-2}$ (90% c.l.; C-stat $_{\nu}$ = 0.94 for 446 d.o.f.). Although the redshift of the burst is unknown, we note that Γ remains unchanged within its 1σ value for $z \lesssim 3$ and we find evidence for intrinsic $N_{\text{H,int}}$ in excess of the Galactic value at 6.5σ confidence. The best-fitting spectral parameters for each of the three data sets and the joint fit are summarized in Table 1.

Applying these parameters to the individual XRT, XMM, and *Chandra* data sets, we calculate the count rate-to-flux conversion factors, and hence their absorbed and unabsorbed fluxes (Table 2). Applying these conversion factors results in the X-ray light curve shown in Figure 1.

2.2.2. Differential Astrometry

In the absence of the detection of an optical afterglow (Section 2.3), we use our *Chandra* observations to refine the *Swift*/XRT position ($1.6''$ uncertainty) to sub-arcsecond accuracy. We perform differential astrometry between our *Chandra* and GMOS observations (Section 2.3). To achieve the maximum signal-to-noise ratio, we combine both epochs of GMOS *i*-band observations and use *SExtractor*⁸ to determine the positions and centroid uncertainty of sources in the field. Performing an absolute astrometric tie to 2MASS using ~ 70 common point sources, we find a resulting rms value of $\sigma_{\text{GMOS-2MASS}} = 0.17''$ ($0.12''$ in each coordinate).

To refine the native *Chandra* astrometry and determine the location of the X-ray afterglow relative to the GMOS image, we perform differential astrometry. We use CIAO routines *mergeall* to combine the two *Chandra* epochs and *wavdetect* to obtain positions and 1σ centroid uncertainties of X-ray sources in the field. We also use *wavdetect* to determine the *Chandra* position of the afterglow from the first epoch and find a 1σ centroid statistical uncertainty $\sigma_{\text{X,ag}} = 0.08''$. We calculate an astrometric tie based on two X-ray and optically bright common sources and find weighted mean offsets of $\delta\text{RA} = -0.27'' \pm 0.06''$ and $\delta\text{Dec} = +0.05'' \pm 0.05''$ giving a tie uncertainty of $\sigma_{\text{CXO-GMOS}} = 0.08''$. There are three additional common, but fainter sources. An astrometric tie using all five sources gives weighted mean offsets and errors of $\delta\text{RA} = -0.29'' \pm 0.15''$ and $\delta\text{Dec} = +0.06'' \pm 0.16''$,

fully consistent with our results from using the two bright sources alone. We therefore use the astrometric solution from the two bright sources only. Applying this solution, we obtain a *Chandra* X-ray afterglow position of $\text{RA}=19^{\text{h}}08^{\text{m}}12.49^{\text{s}}$ and $\text{Dec}=-38^{\circ}00'42.9''$ (denoted by the blue circle in Figure 2) with a total 1σ uncertainty of $0.20''$, accounting for the 2MASS-GMOS astrometric tie, GMOS-*Chandra* tie, and afterglow positional uncertainty. This position is consistent with the XRT position and is offset by $0.94''$ from the XRT centroid.

2.3. Optical Observations and Putative Host Galaxies

We initiated *i*-band observations of GRB 111020A with the Gemini Multi-Object Spectrograph (GMOS) mounted on the Gemini-South 8-m telescope on 2011 October 21.01 UT ($\delta t = 17.7$ hours). The data were reduced using the *gemini/gmos* package in IRAF. In a stack of 9×180 s exposures in $0.74''$ seeing and photometric conditions (Figure 2), we do not detect any sources within the enhanced XRT error circle or coincident with the *Chandra* position. However, the outskirts of the XRT position are partially contaminated by emission from a nearby $i = 17.7$ mag star (S1) and a fainter star (S2) with $i = 22.7$ mag (corrected for $A_i = 0.73$ mag; Figure 2). We detect two additional nearby sources: a faint galaxy (G1) located $2.8''$ away from the center of the *Chandra* position and a brighter galaxy (G2) with a $6.5''$ offset (Figure 2).

To search for a fading optical afterglow, we obtained a second, deeper set of *i*-band observations (11×180 s) with GMOS at $\delta t = 1.74$ days in $0.67''$ seeing. Digital image subtraction using the ISIS software package (Alard 2000) reveals no variation between the two epochs inside or near the X-ray afterglow error circles (Figure 2). To calculate the upper limit on the afterglow, we add several point sources of varying magnitudes between $i = 24$ – 26 mag around the position in the first epoch using IRAF routine *addstar*. We perform photometry in the residual image in $2''$ apertures using the standard published *i*-band zeropoint for GMOS-S and place a 3σ limit on the afterglow of $i \gtrsim 24.4$ mag ($F_{\nu} \lesssim 0.63 \mu\text{Jy}$). We also perform photometry in a $1.8''$ aperture for G1 and a $2.3''$ aperture for G2, giving magnitudes of $i = 23.9 \pm 0.2$ mag and $i = 21.9 \pm 0.1$, respectively (Table 3).

In addition, we obtained *r*-band observations (3×360 s in $0.62''$ seeing) with the Low Resolution Survey Spectrograph 3 (LDSS3) mounted on the Magellan/Clay 6.5-m telescope concurrent to the first epoch of GMOS observations ($\delta t = 17.7$ hours). We easily detect G2, with $r = 21.1 \pm 0.1$ mag, but do not detect G1 to a 3σ limit of $r \gtrsim 23.4$ (corrected for $A_r = 0.99$ mag; Table 3), where the zeropoint is determined from several standard stars at similar airmass.

Since S1 and S2 contaminate the *Chandra* position, we subtract their contribution using point-spread-function (PSF) subtraction on the individual observations and a combined stack of the two GMOS epochs. We use standard PSF-fitting routines in the IRAF *daophot* package. Modelling the PSF using 4 bright, unsaturated stars in the field out to a radius of $3''$ ($\sim 40\text{FWHM}$) from the center of each star, we subtract several stars in the field including S1 and S2. The clean subtraction of these stars indicates a model PSF representative of the PSF of the field. We uncover a faint, mildly extended source (G3) on the outskirts of S1 at coordinates $\text{RA}=19^{\text{h}}08^{\text{m}}12.43^{\text{s}}$ and $\text{Dec}=-38^{\circ}00'43.07''$ (J2000). This source, which lies $0.80''$ from the center of the *Chandra* error circle, has a magnitude of $i = 24.3 \pm 0.2$ and is a potential host of GRB 111020A (Section 3.1). However, we cannot rule out the possibility that this

⁸ <http://sextractor.sourceforge.net/>.

source is a faint star.

2.4. Radio Observations and Possible Afterglow

We observed the position of GRB 111020A with the Expanded Very Large Array⁹ (EVLA) beginning on 1 October 20.95 UT ($\delta t = 16.1$ hours; Program 10C–145) at a mean frequency of 5.8 GHz with a total on-source integration time of 65 min. We observed 3C295 and J1937–1958 for band-pass/flux and gain calibration, respectively, and used standard procedures in the Astronomical Image Processing System (AIPS; Greisen 2003) for data calibration and analysis. With the new wideband capabilities of the EVLA (Perley et al. 2011), our data have an effective bandwidth of ~ 1.5 GHz after excising edge channels and data affected by radio frequency interference. The low declination of GRB 111020A and the compact D configuration of the array at the time of observation caused significant shadowing and required the removal of 7 out of 27 antennas (the north arm of the EVLA).

Taking into account the highly-elongated beam ($33'' \times 7''$ with a position angle of 170°), we detect a 3.7σ source with an integrated flux density of $48 \pm 13 \mu\text{Jy}$ located at RA=19^h08^m12.40^s, Dec=−38°00′41.2″ ($\delta\text{RA} = 1.1''$, $\delta\text{Dec} = 3.6''$, 1σ uncertainty), consistent with the *Chandra* position. The position, peak flux and integrated flux of the source are consistent regardless of our choice of weighting, or if we analyze the upper and lower sidebands separately. However, despite the statistical significance of the detection, we cannot completely rule out sidelobe contribution from nearby bright sources in the field due to the low declination of the burst. Therefore, we conservatively adopt a 3σ upper limit of $39 \mu\text{Jy}$ on the radio afterglow of GRB 111020A for our analysis. We note that if the source is indeed real then upper limits inferred from the radio data can be treated as actual values.

3. RESULTS

3.1. Galaxy Probabilities of Chance Coincidence

To assess which galaxy is the most probable host of GRB 111020A we adopt the methodology of Bloom et al. (2002) and Berger (2010) to calculate the probability of chance coincidence $P(< \delta R)$ at a given angular separation δR . We determine the expected number density of galaxies brighter than a measured apparent magnitude, m , using the results of deep optical galaxy surveys (Hogg et al. 1997; Beckwith et al. 2006):

$$\sigma(\leq m) = \frac{1}{0.33 \times \ln(10)} \times 10^{0.33(m-24)-2.44} \text{ arcsec}^{-2}. \quad (1)$$

Then the probability of chance coincidence is given by (Bloom et al. 2002)

$$P(< \delta R) = 1 - e^{-\pi(\delta R)^2 \sigma(\leq m)}. \quad (2)$$

We calculate $P(< \delta R)$ for each of the three host galaxy candidates (Figure 3), and find that G3 is the most probable host of GRB 111020A with $P(< \delta R) = 0.01$, while for G1 and G2, the values are $P(< \delta R) = 0.10$ and 0.12 , respectively.

3.2. X-ray Light Curve Fitting and a Jet Break

The temporal behavior of the X-ray afterglow flux is characterized by a steady power-law decline until $\delta t \approx 2$ days when there is a significant steepening in the light curve (Figure 1). A single power law model with a decline rate determined by the X-ray data at early times ($t \lesssim 2$ days) provides a poor fit to the late-time data (dotted line in Figure 1); in particular, it overestimates the *Chandra* detection and upper limit. To quantitatively assess the shape of the X-ray light curve, we therefore invoke a broken power law model, given by

$$F_X = F_{X,0} \left[\left(\frac{t}{t_j} \right)^{\alpha_{X,1}s} + \left(\frac{t}{t_j} \right)^{\alpha_{X,2}s} \right]^{1/s}, \quad (3)$$

where $F_{X,0} = 2^{1/s} F_X(t = t_j)$, $\alpha_{X,1}$ and $\alpha_{X,2}$ are the power law indices pre- and post-break, respectively, t_j is the break time in seconds, and s is a dimensionless smoothness parameter that characterizes the sharpness of the break. We perform a three-parameter χ^2 -grid search over $F_{X,0}$, $\alpha_{X,1}$ and t_j . If we use a relatively sharp break (e.g. $s \approx -10$), the *Chandra* 3σ upper limit constrains $\alpha_{X,2} \lesssim -1.7$. If we allow for a smoother break (e.g. $s \approx -1$), $\alpha_{X,1}$ remains unchanged but the break occurs at later times ($t_j \approx 4$ days) and $\alpha_{X,2}$ is required to have a steeper value of $\lesssim -2.2$ to accommodate the *Chandra* upper limit. This scenario generally provides a poorer fit to the last *Chandra* and *Swift*/XRT points. We therefore adopt the sharp-break scenario. Fixing $s = -10$ and $\alpha_{X,2} = -2.1$, we find a best-fit broken power law model characterized by $F_X(t_j) = (1.36 \pm 0.45) \times 10^{-13} \text{ erg cm}^{-2} \text{ s}^{-1}$, $\alpha_{X,1} = -0.78 \pm 0.05$, and $t_j = 2.0 \pm 0.5$ days (1σ , $\chi^2_\nu = 1.1$ with 15 d.o.f.; Figure 1). This best-fit model is shown in Figure 1. The best fit parameters are independent of our choice of $\alpha_{X,2}$ between -1.7 and -3 . We also note the presence of a slight flux enhancement relative to the power law decay at $\delta t \approx 3 \times 10^4 \text{ s}$ (0.35 days). If we remove these points from our fits, the resulting best-fit parameters remain unaffected.

The required change in the temporal index is $\Delta\alpha_{12} \gtrsim 0.9$. There are several possibilities that can explain breaks in GRB afterglow light curves. The first scenario is the transition of the cooling frequency across the band, but this only predicts $\Delta\alpha = 0.25$ (Sari et al. 1998). An alternative possibility is the cessation of energy injection, either from refreshed shocks or a long-lasting central engine (e.g., Rees & Meszaros 1998; Sari & Mészáros 2000; Zhang & Mészáros 2002), which has been used to explain the termination of a shallow decay or plateau phase in the X-ray and optical light curves of several long GRBs. However, these cases all exhibit earlier temporal breaks at $\sim 10^3 - 10^4 \text{ sec}$ with $\Delta\alpha_{12} \sim 0.7$ ($\alpha_{X,1} \approx -0.5$, $\alpha_{X,2} \approx -1.2$; Nousek et al. 2006; Zhang et al. 2006; Liang et al. 2007). Attributing the break in GRB 111020A to the cessation of central engine activity would require sustained energy injection from the start of XRT monitoring to the break time, ~ 100 seconds to 2 days, whereas the timescales of energy injection for long GRBs are \lesssim few hours (Nousek et al. 2006; Zhang et al. 2006; Liang et al. 2007; Racusin et al. 2009). Single episodes of energy injection have also been observed in two short GRBs: 051221A and 050724A (Berger et al. 2005; Soderberg et al. 2006; Burrows et al. 2006; Grupe et al. 2006)). The light curve of GRB 051221A, which exhibits a power law decay with index $\alpha_{X,1} = -1.1$, a plateau, and a return to the same power law ($\Delta\alpha_{12} = 0$), is interpreted as a single period of energy injection (Soderberg et al. 2006;

⁹ Newly renamed the Karl G. Jansky Very Large Array.

Burrows et al. 2006). A super-imposed flare on the light curve of GRB 050724A with a single underlying decay index of $\alpha_{X,1} = -0.98$ is also possibly related to late-time reactivation of the central engine (Berger et al. 2005; Grupe et al. 2006; Figure 1). Neither of these light curves resemble the behavior of GRB 111020A, where the change in slope is substantially greater.

Yet another possibility to explain the break is a sharp change in the external density. However, models for density jumps in a uniform medium (Nakar & Granot 2007) predict that the density would need to decrease by greater than a factor of $\sim 10^3$ to account for the observed $\Delta\alpha_{12} > 0.9$ steepening. More realistic density contrasts of ~ 10 predict $\Delta\alpha_{\max} \approx 0.4$ in optical and X-ray afterglow light curves (Nakar & Granot 2007).

Finally, we consider that the observed steepening is a jet break, when the edge of a relativistically-beamed outflow becomes visible to the observer and the jet spreads laterally (Sari et al. 1999; Rhoads 1999). This model is often adopted to explain $\Delta\alpha_{12} \sim 1$ in the light curves of long GRBs (e.g., Frail et al. 2001; Bloom et al. 2003; Racusin et al. 2009) and has been observed in one other short burst, GRB 051221A ($\Delta\alpha_{12} \sim 0.9$, Figure 1; Soderberg et al. 2006; Burrows et al. 2006). Given the similarity in $\Delta\alpha_{12}$ and the timescales of jet breaks in both short and long GRBs, we conclude that the observed steepening in the light curve of GRB 111020A is best explained by a jet break at $t_j = 2.0 \pm 0.5$ days.

3.3. Afterglow Properties

We utilize our radio, optical and X-ray observations to constrain the explosion properties and circumburst environment of GRB 111020A. In particular, we adopt the standard synchrotron model for GRB afterglows (Sari et al. 1998; Granot & Sari 2002) which provides a mapping from observable properties to the isotropic-equivalent kinetic energy ($E_{K,\text{iso}}$), circumburst density (n_0), and the fractions of post-shock energy in radiating electrons (ϵ_e) and magnetic fields (ϵ_B). We use data at the time of the radio and first optical observations ($\delta t = 17.7$ hours), as well as the decay indices from the full X-ray light curve.

First, we constrain the electron power-law index p , using a combination of temporal and spectral information. From the X-ray light curve, we measure $\alpha_{X,2} \lesssim -1.7$ (Section 3.2). For $p = -\alpha_{X,2}$, appropriate for a spreading jet (Sari et al. 1999), we can then constrain $p \gtrsim 1.7$. To further constrain p and investigate the location of the cooling frequency, ν_c , we compare the values $\alpha_{X,1} = -0.78 \pm 0.05$ and $\beta_X = -1.04 \pm 0.16$ ($\beta_X = 1 - \Gamma$; 1 σ) to the closure relations for a relativistic blastwave in a constant density ISM-like medium for $p > 2$, a typical environment expected for a short GRB from a non-massive star progenitor (Sari et al. 1999; Granot & Sari 2002). If $\nu_c > \nu_X$ then the independently-derived values for p from the temporal and spectral indices are inconsistent: $p = 2.0 \pm 0.07$ from $\alpha_{X,1}$, and $p = 3.1 \pm 0.32$ from β_X (errors are 1σ).

However, if $\nu_c < \nu_X$ we obtain $p = 1.7 \pm 0.07$ from $\alpha_{X,1}$, (Granot & Sari 2002) which is consistent with the p value inferred from $\alpha_{X,2}$, but yields a divergent total integrated energy in electrons unless a break at high energies in the distribution is invoked. Although a flat electron distribution ($p < 2$) is possible and not uncommon (e.g. Dai & Cheng 2001; Panaitescu & Kumar 2001; Racusin et al. 2009), the standard relations for $1 < p < 2$ yield $p = 0.84 \pm 0.25$ from $\alpha_{X,1}$. This solution is not self-consistent, and would also require an unusually sharp break of $\Delta p \gtrsim 1.2$ in the electron distribution.

Continuing with the assumptions that $\nu_c < \nu_X$ and $p > 2$, we obtain $p = 2.1 \pm 0.32$ from β_X , which is marginally consistent with the value inferred from the temporal index. Put another way, $\alpha - 3\beta/2 = 0.77 \pm 0.30$, which satisfies the closure relation for $\nu_c < \nu_X$ (Sari et al. 1998). We therefore conclude that $\nu_c < \nu_X$. We note that the spectral index is generally more reliable in the determination of p because it remains constant over time and is not subject to alternative processes such as energy injection or flaring. In this case, the same β_X was also independently determined from both the XMM and XRT data sets (Table 1). Therefore for the rest of our calculations, we take a reasonable value of $p = 2.1$ as determined from β_X .

We next determine a set of constraints on n_0 and $E_{K,\text{iso}}$ based on the X-ray flux density, radio limit, and the condition that $\nu_c < \nu_X$. First, we use the X-ray afterglow emission as a proxy for $E_{K,\text{iso}}$ assuming the X-ray emission is from the forward shock. For $\nu_c < \nu_X$ at the time of our broad-band observations ($\delta t = 17.7$ hours), we use $F_X = 0.032 \mu\text{Jy}$ at $\nu_X = 2.4 \times 10^{17}$ Hz (1 keV), and $p = 2.1$ to obtain (Granot & Sari 2002)

$$E_{K,\text{iso}} \approx 2.2 \times 10^{50} (1+z)^{-1} \epsilon_e^{-1.07} \epsilon_B^{-0.024} d_{L,28}^{1.95} \text{ erg} \quad (4)$$

where $d_{L,28}$ is the luminosity distance in units of 10^{28} cm. Next, we use $E_{K,\text{iso}}$ to constrain n_0 . Using our 3σ EVLA limit of $F_{\nu,\text{rad}} \lesssim 39 \mu\text{Jy}$, we can determine an upper limit on n_0 under the reasonable assumption that our observed radio band ($\nu = 5.8$ GHz) is above the self-absorption frequency ($\nu_a < \nu_{\text{rad}} < \nu_m$; $F_{\nu,\text{rad}} \propto n_0^{1/2}$) at the time of observations. For this scenario (Granot & Sari 2002),

$$n_0 \lesssim 1.7 \times 10^{-3} E_{K,\text{iso},52}^{-5/3} (1+z)^{-5/3} d_{L,28}^4 \epsilon_e^{4/3} \epsilon_B^{-2/3} \text{ cm}^{-3}, \quad (5)$$

where $E_{K,\text{iso},52}$ is in units of 10^{52} erg and n_0 is in cm^{-3} . As noted in Section 2.4, if the marginal radio detection is indeed real, then this upper bound can be replaced with an equality. Finally, we can place a lower limit on the density using the condition that $\nu_c < \nu_X$ (i.e., $\nu_c \lesssim 2.4 \times 10^{16}$ Hz; 0.1 keV)

$$n_0 \gtrsim 4.5 \times 10^{-4} (1+z)^{-1/2} \epsilon_B^{-3/2} E_{K,\text{iso},52}^{-1/2} \text{ cm}^{-3}. \quad (6)$$

It is clear that $E_{K,\text{iso}}$ and n_0 depend sensitively on our choice of z , ϵ_e and ϵ_B . The fractions ϵ_e, ϵ_B are not expected to exceed $\sim 1/3$. We therefore calculate $E_{K,\text{iso}}$ for two cases: I: $\epsilon_e = \epsilon_B = 1/3$, and II: more typical values of $\epsilon_e = \epsilon_B = 0.1$. We then calculate the range of allowed n_0 set by Equations 5 and 6, which becomes wider as the redshift increases. For Case I, this requires that $z \gtrsim 0.2$, below which the constraints on n_0 conflict (Figure 4). At the median observed redshift of the short GRB population, $z \sim 0.5$, we obtain $E_{K,\text{iso}} \approx 3.7 \times 10^{50}$ erg and $n_0 = 0.01 - 0.06 \text{ cm}^{-3}$. For Case II, the constraints on n_0 require a higher redshift of $z \gtrsim 1.5$ (Figure 4). For a fiducial redshift of $z = 1.5$, we obtain $E_{K,\text{iso}} \approx 1.2 \times 10^{52}$ erg and $n_0 = 0.008 \text{ cm}^{-3}$. The parameters for the two cases are listed in Table 4. Although we cannot distinguish between these two scenarios, both cases require low circumburst densities of $n \sim 0.01 \text{ cm}^{-3}$.

3.4. Jet Opening Angle

In the context of a jet break, we use the time of the break from the X-ray light curve (2.0 ± 0.5 days) and the circumburst density and energy estimates from the previous section to constrain θ_j . The time of the break is a direct reflection of the jet opening angle (Sari et al. 1999; Frail et al. 2001),

$$\theta_j = 0.1 t_{j,d}^{3/8} (1+z)^{-3/8} E_{K,iso,52}^{-1/8} n_0^{1/8} \quad (7)$$

where $t_{j,d}$ is expressed in days. For our fiducial Case I ($z = 0.5$, $\epsilon_e = \epsilon_B = 1/3$), $E_{K,iso} \approx 3.7 \times 10^{50}$ erg and $n \approx 0.01 - 0.06$ cm $^{-3}$ give $\theta_j = 7 - 8^\circ$. This leads to a beaming correction on the energy of $f_b \equiv [1 - \cos(\theta_j)] = 0.007 - 0.01$, and therefore a true kinetic energy $E_K = f_b E_{K,iso} \approx (3 - 4) \times 10^{48}$ erg (Table 4). To estimate the beaming-corrected γ -ray energy, we infer $E_{\gamma,iso}$ from the *Swift*/BAT fluence and apply a bolometric correction factor of 5 to roughly convert to a representative observed γ -ray energy range of $\sim 10 - 1000$ keV. This factor is derived from short GRBs observed by satellites with wider energy coverage (Berger 2010; Margutti et al. 2012). We obtain $E_{\gamma,iso} = 2.1 \times 10^{50}$ erg and therefore a true γ -ray energy of $E_\gamma \approx 2 \times 10^{48}$ erg.

For Case II ($z = 1.5$, $\epsilon_e = \epsilon_B = 0.1$), where $n_0 \approx 0.008$ cm $^{-3}$ and $E_{K,iso} \approx 1.2 \times 10^{52}$ erg, we obtain a smaller opening angle of $\theta_j \approx 3^\circ$. This leads to $f_b \approx 1.4 \times 10^{-3}$ and hence, $E_\gamma \approx 3 \times 10^{48}$ erg and $E_K \approx 2 \times 10^{49}$ erg.

In both cases, the true γ -ray energy is few $\times 10^{48}$ erg while the kinetic energy is an order of magnitude higher at $z = 1.5$ than at $z = 0.5$. This results in a lower γ -ray conversion efficiency ($\eta_\gamma \equiv E_\gamma/E_{tot}$) for Case II of 0.15 compared to 0.3–0.4 for Case I (Table 4). The total energy even for Case II is $\sim 10 - 100$ times lower than for long GRBs.

3.5. Extinction

We investigate the presence of extinction by comparing the unabsorbed X-ray flux and the optical non-detection at $\delta t = 17.7$ hour. Since we do not know the exact location of the cooling frequency, we assume a maximum value $\nu_{c,max}$ of 2.4×10^{17} Hz (1 keV) and extrapolate the X-ray flux to the optical band using the shallowest possible slope of $\beta = -(p-1)/2 = -0.55$ to obtain the lowest bound on the expected optical afterglow flux in the absence of extinction; any other assumption for the location of $\nu_c < \nu_X$ would result in a higher predicted optical flux density. For $p = 2.1$ we estimate $F_{\nu,opt} \approx 1.1$ μ Jy ($i = 23.8$ mag). Given that our observed 3σ upper limit is $i \gtrsim 24.4$ mag, this implies a lower limit on the optical extinction in excess of the Galactic value of $A_i \gtrsim 0.6$ mag 10 . In the rest frame of the burst for a Milky Way extinction curve, this translates to $A_V^{host} \gtrsim 0.6$ mag for $z = 0.5$ and $A_V^{host} \gtrsim 0.2$ at $z = 1.5$ (Cardelli et al. 1989). Using Galactic relations between N_H and A_V , $N_{H,int}/A_V \approx (1.7 - 2.2) \times 10^{21}$ (Predehl & Schmitt 1995; Watson 2011), we infer lower limits of $N_{H,int} \gtrsim 10^{21}$ cm $^{-2}$ at $z = 0.5$ and $N_{H,int} \gtrsim 4.4 \times 10^{20}$ cm $^{-2}$ at $z = 1.5$, consistent with our value of 7.5×10^{21} cm $^{-2}$ ($z = 0$) derived from the X-ray spectrum (Table 1). However, an appreciable extinction is unexpected given the burst's location on the outskirts of its potential host galaxy. We note that the burst is located at Galactic coordinates $(l, b) = (359.3^\circ, -19.4^\circ)$ which is toward the Galactic Bulge on a steep gradient in the dust map (Schlegel et al. 1998) and thus may be subject to substantial ($\sim 30\%$) uncertainties in the Galactic extinction 11 . Taking this uncertainty into account reduces the required

¹⁰ We note that for $p \lesssim 1.9$, no host galaxy extinction is required

¹¹ Using a high-resolution ($\theta_{FWHM} = 15''$) WISE 12μ m map, we do not see strong evidence for any thin dust filaments at the location of the burst which would result in $> 30\%$ uncertainties in the Galactic A_V (D. Finkbeiner, private comm.)

A_V^{host} to $\gtrsim 0.2 - 0.3$ mag depending on the redshift of the burst.

4. DISCUSSION

4.1. Environment

From our broad-band observations, we constrain the circumburst density of GRB 111020A to $n_0 \sim 0.01$ cm $^{-3}$ which is consistent with the low values inferred for a few previous short GRBs (Soderberg et al. 2006; Panaitescu 2006; Stratta et al. 2007; Perley et al. 2009b; Berger 2010; Fong et al. 2011). The inferred density fits well with the framework of NS-NS/NS-BH binary progenitor systems, which may be subject to substantial kicks from their host galaxies and are predicted to typically occur at densities of $\sim 10^{-6} - 1$ cm $^{-3}$ (Perna & Belczynski 2002; Belczynski et al. 2006).

GRB 111020A has an offset of $\approx 0.80''$ from its most probable host galaxy (G3; Figure 2). For redshifts between $z = 0.5 - 1.5$, this translates to a projected physical offset of $\approx 5 - 7$ kpc, which is comparable to the median value of ~ 5 kpc for well-localized short GRBs with host associations (Fong et al. 2010; Church et al. 2011). Although G3 has the lowest probability of chance coincidence by an order of magnitude (Figure 3), we cannot rule out the possibility that G3 is a faint star. The next most probable galaxies, G1 and G2, are situated $2.8''$ ($17 - 24$ kpc) and $6.5''$ ($40 - 56$ kpc), respectively, from GRB 111020A (Figure 2). If the burst originated from one of these galaxies, this would put GRB 111020A at the high end of the observed offset distribution, similar to the growing sub-class of apparently “hostless” short GRBs which likely occur $\gtrsim 30$ kpc from their host galaxies (Berger 2010). All of these inferred offsets are consistent with predicted offset distributions of NS-NS/NS-BH binaries originating in Milky Way-type galaxies (Bloom et al. 1999; Fryer et al. 1999; Belczynski et al. 2006; Salvaterra et al. 2010).

Most short GRB host galaxies with confirmed spectroscopic redshifts have measured luminosities of $L_B \approx 0.1 - 1 L_*$ (Berger et al. 2007). The apparent magnitude of G3 is $i \approx 24.3$, which corresponds to $L_B \approx 0.1 - 1 L_*$ over $z \approx 0.5 - 2.3$ when compared to the luminosity function of galaxies at corresponding redshifts in the DEEP2 and LBG surveys (Willmer et al. 2006; Reddy & Steidel 2009). This is consistent with the redshift range inferred from the afterglow.

We next investigate the nature of the dust and gas in the environment of GRB 111020A through an analysis of A_V^{host} and $N_{H,int}$. We have shown that the burst requires dust extinction of $A_V^{host} \gtrsim 0.2 - 0.6$ mag, depending on the redshift of the burst and the uncertainty in Galactic extinction. We have also measured a neutral Hydrogen column density intrinsic to the burst environment of $N_{H,int} = (7.5 \pm 2.0) \times 10^{21}$ cm $^{-2}$ at $z = 0$, which becomes higher for any other choice of z . High values of both dust extinction and X-ray absorption have been linked to “dark” GRBs (e.g. Perley et al. 2009a; Campana et al. 2011) which have optically sub-luminous afterglows compared to their X-ray or NIR counterparts and can quantitatively be classified by $|\beta_{ox}| \lesssim |\beta_X| - 0.5$ (van der Horst et al. 2009; see also Jakobsson et al. 2004). With $|\beta_X| = 1.0$ and $|\beta_{ox}| \lesssim 0.46$, GRB 111020A is consistent with this definition of dark GRBs. While optical extinction intrinsic to long GRB environments is not uncommon and commensurate with their origin in dusty, star-forming regions, evidence for substantial extinction has been reported for only one other short

burst, GRB 070724A, which required $A_V^{\text{host}} \gtrsim 2$ mag to explain the suppression of optical emission relative to the NIR (Berger et al. 2009; Kocevski et al. 2010). The location of GRB 070724A on the outskirts of its host galaxy, ~ 5 kpc from the center, suggested either an origin in a star-forming region or a progenitor system which produced the dust itself (Berger et al. 2009). The potentially appreciable extinction and the location with respect to its putative host suggests that the same conclusions may be drawn for GRB 111020A.

On the other hand, the relation between $N_{\text{H,int}}$ and the darkness of a burst is less clear. A recent study of long dark GRBs shows them to have higher intrinsic column densities than non-dark GRBs, which suggests that the darkness of a burst is largely due to absorption by circumburst material (Campana et al. 2011). To investigate this relationship for GRB 111020A, we extract spectra and best-fitting $N_{\text{H,int}}$ for all short GRBs with XRT-detected afterglows in the same manner as GRB 111020A (see Section 2.2.1), over time ranges with no evidence for spectral evolution. There are 22 short bursts with sufficient X-ray counts to perform spectral analysis, 11 of which have known redshifts (Table 5). We find a short GRB weighted average of $N_{\text{H,int}}(z=0) = (1.1 \pm 0.14) \times 10^{21} \text{ cm}^{-2}$ (90% c.l.; Figure 5). In comparison, GRB 111020A has a high value of $N_{\text{H,int}} = (7.5 \pm 2.0) \times 10^{21} \text{ cm}^{-2}$ at $z=0$ (Figure 5). Taken at face value, it is surprising to find a large $N_{\text{H,int}}$ for a substantial offset, and may suggest that the burst occurred in a relatively metal-rich environment.

4.2. Beaming, Energetics, and Rates

We uncover a break in the X-ray light curve of GRB 111020A at ≈ 2 days, which we interpret as a jet break (Section 3.2). Depending on our values for z , ϵ_e and ϵ_B , we infer an opening angle of $\approx 3-8^\circ$. This is reminiscent of the first jet break discovery in GRB 051221A, with $\theta_j \approx 7^\circ$ (Soderberg et al. 2006; Burrows et al. 2006), and suggests that at least a fraction of these events are highly collimated. In addition, temporal breaks at $t_j \lesssim$ few hours in GRBs 061201 (Stratta et al. 2007) and 090510 (De Pasquale et al. 2010; Nicuesa Guelbenzu et al. 2012), if interpreted as jet breaks, lead to $\theta_j \approx 1^\circ$ (Figure 6). However, these two cases resemble early breaks in long GRBs that are generally attributed to the cessation of energy injection, and not collimation.

Although the remaining short GRB afterglow data is sparse, the lack of observed jet breaks in their X-ray light curves can be used to place lower limits on the opening angles. Indeed, *Chandra* observations of GRB 050724A out to 22 days indicated $\theta_j \gtrsim 25^\circ$, consistent with a spherical explosion (Grupe et al. 2006). A recent study by Coward et al. (2012) analyzed the sample of short GRB *Swift*/XRT light curves up to August 2011 with monitoring $\gtrsim 1$ day which included 6 additional events, and inferred $\theta_j \gtrsim 6-16^\circ$, assuming $n_0 = 1 \text{ cm}^{-3}$ for all bursts. We revise this analysis for 3 of the events with robust X-ray light curves (GRBs 070714B, 070724A, 071227; data analysis prescriptions from Margutti et al. 2012) employing a more representative $n_0 \approx 10^{-2} \text{ cm}^{-3}$ (e.g. Soderberg et al. 2006 and this work). We derive $E_{\gamma,\text{iso}}$ from the reported fluences, applying a bolometric correction when necessary to represent an energy range of $\sim 10-1000$ keV, and infer more realistic lower limits of $\gtrsim 2-6^\circ$ (Figure 6). These limits are indeed lower than the detected values for GRBs 051221A and 111020A, and therefore do not add strong constraints on the distribution. We caution that the sample presented here represents only the $\sim 30\%$

of the *Swift* short GRB population that have bright X-ray afterglows and relatively slow flux decline rates; the remaining fraction do not have detectable X-ray afterglows or fade too quickly so constraints cannot be placed on their collimation.

There are now two short GRBs with opening angle measurements, two with measurements based on more tentative early breaks, and an additional four with lower limits (Figure 6). These early constraints create a distribution that may mimic the distribution for long GRBs, which ranges from $\sim 2-20^\circ$ with a median of 7° (Figure 6; Frail et al. 2001; Berger et al. 2003; Bloom et al. 2003; Ghirlanda et al. 2004; Friedman & Bloom 2005; Racusin et al. 2009; Cenko et al. 2010; Filgas et al. 2011; Goldstein et al. 2011; Cenko et al. 2011). More events are needed to assess the real differences between the distributions. However, simulations of post-merger black hole accretion predict jets with $\theta_j \sim 5-20^\circ$ (Aloy et al. 2005; Rosswog 2005; Rezzolla et al. 2011) to several tens of degrees (Ruffert & Janka 1999b; Rezzolla et al. 2011) depending on the mechanism of energy extraction and Lorentz factor, so there are expectations on theoretical grounds that the short GRB distribution is wider.

The first major ramification of collimation is the correction to the total energy release: the true energy is lower than the isotropic-equivalent value by the beaming factor, f_b . For GRB 111020A with an opening angle of $\approx 3-8^\circ$, this correction factor is substantial, $0.001-0.01$. Depending on the redshift, the beaming-corrected energy of GRB 111020A is $E_\gamma \approx (2-3) \times 10^{48} \text{ erg}$ (Table 4) which is an order of magnitude lower than for GRB 051221A with $E_\gamma \approx (1-2) \times 10^{49} \text{ erg}$ (Soderberg et al. 2006; Burrows et al. 2006) and GRB 050724A with $E_\gamma \approx (0.4-4) \times 10^{50} \text{ erg}$ (Grupe et al. 2006). The three remaining events with opening angle lower limits, GRBs 070714B, 070724A and 071227, have ranges of $E_\gamma \approx 10^{48}-10^{51} \text{ erg}$, where the upper bound is set by the isotropic-equivalent γ -ray energy in the $\approx 10-1000$ keV band. The small population of short GRBs with measured E_γ therefore has a median value of $E_\gamma \sim 10^{49} \text{ erg}$, which is an order of magnitude below *Swift* long GRBs (Kocevski & Butler 2008; Racusin et al. 2009) and 2 orders of magnitude below the pre-*Swift* population (Frail et al. 2001; Bloom et al. 2003). Again, this sample is incomplete because we can only measure E_γ for bursts with well-constrained opening angles.

In a similar vein, we compare the beaming-corrected kinetic energy and total energy (E_K , E_{tot}) of GRB 111020A to the values for other short bursts. Because $E_{K,\text{iso}}$ is more sensitive to our choices for z , ϵ_e and ϵ_B , we infer different values for Case I and II. For Case I, we infer $E_K \approx (3-4) \times 10^{48} \text{ erg}$, $E_{\text{tot}} = E_\gamma + E_K \approx (5-6) \times 10^{48} \text{ erg}$, and $\eta_\gamma \approx 0.3-0.4$. For Case II, we calculate $E_K \approx 2 \times 10^{49} \text{ erg}$, $E_{\text{tot}} \approx 2 \times 10^{49} \text{ erg}$ and $\eta_\gamma \approx 0.15$. GRB 051221A had $E_K \approx 8 \times 10^{48} \text{ erg}$ and a total energy release of $\approx 2.5 \times 10^{49} \text{ erg}$ (Soderberg et al. 2006; Burrows et al. 2006) while GRB 050724A had a total energy of $10^{50}-10^{51} \text{ erg}$. With $E_{\text{tot}} \approx (0.5-2) \times 10^{49} \text{ erg}$, GRB 111020A may be on the low end of the total energy distribution, but more events with beaming-corrected energies are needed to better characterize the distribution for short GRBs.

The true total energy release of short GRBs has strong implications on the energy extraction mechanism. Two primary mechanisms, the thermal energy release from $\nu\bar{\nu}$ annihilation in a baryonic outflow (Jaroszynski 1993; Mochkovitch et al. 1993) and magnetohydrodynamic (MHD) processes in the black hole's accretion remnant (e.g. Blandford & Znajek

1977; Rosswog et al. 2003), give different estimates for the expected energy release. Predictions for $\nu\bar{\nu}$ annihilation are largely dependent on the mass of the disc and efficiency to produce pairs. Simulations of an outflow due to $\nu\bar{\nu}$ annihilation suggest beaming-corrected total energy releases could reach $10^{48} - 10^{49}$ erg (Ruffert & Janka 1999b,a; Popham et al. 1999; Rosswog 2005; Birkel et al. 2007; Lee & Ramirez-Ruiz 2007). Higher energy releases can be obtained from MHD processes, which can produce luminosities of $\gtrsim 10^{52}$ erg s $^{-1}$ ($\gtrsim 10^{50}$ erg s $^{-1}$ when corrected for beaming; Popham et al. 1999; Rosswog et al. 2003; Lee & Ramirez-Ruiz 2007) depending on the nature of the magnetic field amplification. While the true energy releases of GRBs 051221A and 050724A suggest that MHD processes may be powering these events (Berger et al. 2005; Grupe et al. 2006; Soderberg et al. 2006; Burrows et al. 2006), the total energy of GRB 111020A is consistent with predictions for both scenarios.

The second major consequence of beaming is that the true event rate is *higher* than the observed rate by the inverse of the beaming factor (i.e., $R_{\text{true}} = f_b^{-1} R_{\text{obs}}$). Thus, beaming provides essential information for understanding the relation to various progenitor systems and is of particular interest since the NS-NS/NS-BH merger rates, which are a critical input for estimates of Advanced LIGO gravitational wave detections, are highly uncertain (e.g., Abadie et al. 2010; Metzger & Berger 2012). The current estimated *observed* short GRB volumetric rate is ~ 10 Gpc $^{-3}$ yr $^{-1}$ (Nakar et al. 2006). The estimated NS-NS merger rate is much higher: ~ 200 – 3000 Gpc $^{-3}$ yr $^{-1}$ (Kalogera et al. 2004; Nakar et al. 2006).

The discrepancy in these rates can be explained if short GRBs have typical $\theta_j \sim 8^\circ$ ($f_b^{-1} \sim 100$; see also Metzger & Berger 2012). The determination of GRB 111020A's opening angle of $3 - 8^\circ$ ($f_b^{-1} = 100 - 730$), along with the small but increasing sample of opening angle constraints for short GRBs, implies that at least a fraction of these events are significantly beamed and that the true rate of short GRBs is at least $\sim 100 - 1000$ Gpc $^{-3}$ yr $^{-1}$. With a few additional opening angle measurements, this value can be significantly improved. Other proposed progenitor models, e.g., WD-WD mergers or accretion-induced collapse of a WD/NS (Qin et al. 1998; Levan et al. 2006; Metzger et al. 2008) have estimated rates of $\lesssim 1000$ Gpc $^{-3}$ yr $^{-1}$ and $\sim 0.1 - 100$ Gpc $^{-3}$ yr $^{-1}$, respectively (Lee & Ramirez-Ruiz 2007; Darbha et al. 2010), so if a large fraction of short GRBs have opening angles of $\lesssim 25^\circ$, these systems may not contribute significantly to the progenitor population.

5. CONCLUSIONS AND FUTURE WORK

We have presented observations of GRB 111020A, utilizing extensive coverage in the X-rays with *Swift*/XRT, XMM and *Chandra* to uncover a temporal break, most naturally explained as a jet break. Our limit on the radio afterglow from EVLA combined with the inference that $\nu_c < \nu_x$ leads to a robust range on the circumburst density of $\sim 0.01 - 0.1$ cm $^{-3}$. The jet break time of ≈ 2 days leads to an opening angle of $3 - 8^\circ$, depending on the redshift and equipartition fractions, which leads to beaming-corrected energies of $E_\gamma \approx (2 - 3) \times 10^{48}$ erg, $E_K \approx (0.3 - 2) \times 10^{49}$ erg and $E_{\text{tot}} \approx (0.5 - 2) \times 10^{49}$ erg. This result, along with the previous jet break constraints for GRBs 051221A and 050724A suggests that there may be a spread in true energy release, $\sim 10^{48} - 10^{50}$ erg for short GRBs (Berger et al. 2005; Grupe et al. 2006; Soderberg et al. 2006; Burrows et al. 2006).

Furthermore, our optical observations provide a limit on the

afterglow and enabled the discovery of a putative host galaxy with $i \approx 24.3$ mag. A comparison of the X-ray and optical data at $\delta t = 17.7$ hours provides a lower limit on the host galaxy extinction of $A_V^{\text{host}} \gtrsim 0.2 - 0.6$ mag. This is consistent with the high intrinsic column density from X-ray absorption when compared to the mean for the short GRB population.

GRB 111020A demonstrates that rapid multi-wavelength follow-up is vital to our understanding of the basic properties of short GRBs: the geometry, energetics, and circumburst densities. In particular, the search for jet breaks on timescales of \gtrsim few days is imperative for placing meaningful constraints on the opening angle distribution. Ideally, the detection of breaks in both optical and X-ray data leads to an unambiguous and tight constraint on the opening angle; however, optical afterglows are only detected in $\sim 30\%$ of *Swift* short GRBs, while X-ray afterglows have been detected in $\sim 70\%$. Furthermore, optical afterglows are intrinsically faint and subject to host galaxy contamination, making long-term monitoring highly challenging. Therefore, the jet break search is optimized in the X-ray band where the burst is not subject to such contamination and the afterglow brightness is virtually independent of the typically low circumburst densities. The X-rays also allow for a measurement of the kinetic energy of the outflow. Deep radio limits provide additional constraints on the circumburst density and energy. The EVLA upgrade is now enabling us to probe events with relatively low energy scales of $\sim 10^{48}$ erg and densities of $\lesssim 10^{-2}$ cm $^{-2}$.

The collimation of short GRBs will undoubtedly further our knowledge of their true energetics and rates. While the former provides information on the explosion and energy extraction mechanisms, the latter is crucial for understanding the relation to various progenitor systems (e.g., NS-NS mergers). Significant improvement on the estimated short GRB observed rate of ~ 10 Gpc $^{-3}$ yr $^{-1}$ (Nakar et al. 2006) will have a critical impact on estimates for coincident short GRB-gravitational wave detections in the era of Advanced LIGO/VIRGO (Abadie et al. 2010). The uncertainty in the observed short GRB rate is dominated by the uncertainty in the beaming fraction and with only a handful of short GRB opening angles measured to date, the discovery of even a few additional jet breaks in the coming years will enable significant progress.

We thank D. Finkbeiner for helpful discussions. The Berger GRB group at Harvard is supported by the National Science Foundation under Grant AST-1107973. Partial support was also provided by the National Aeronautics and Space Administration through Chandra Award Number GO1-12072X issued by the Chandra X-ray Observatory Center, which is operated by the Smithsonian Astrophysical Observatory for and on behalf of the National Aeronautics Space Administration under contract NAS8-03060. Additional support was provided by NASA/Swift AO6 grant NNX10AI24G. Observations were obtained with the EVLA (program 10C-145) operated by the National Radio Astronomy Observatory, a facility of the National Science Foundation operated under cooperative agreement by Associated Universities, Inc. This paper includes data gathered with the 6.5 meter Magellan Telescopes located at Las Campanas Observatory, Chile. This work is based in part on observations obtained at the Gemini Observatory, which is operated by the Association of Universities for Research in Astronomy, Inc., under a cooperative agreement with the NSF on behalf of the Gemini partnership:

the National Science Foundation (United States), the Science and Technology Facilities Council (United Kingdom), the National Research Council (Canada), CONICYT (Chile), the

Australian Research Council (Australia), Ministério da Ciência, Tecnologia e Inovação (Brazil) and Ministerio de Ciencia, Tecnología e Innovación Productiva (Argentina).

REFERENCES

- Abadie, J., et al. 2010, *Classical and Quantum Gravity*, 27, 173001
- Alard, C. 2000, *A&AS*, 144, 363
- Aloy, M. A., Janka, H.-T., & Müller, E. 2005, *A&A*, 436, 273
- Beckwith, S. V. W., et al. 2006, *AJ*, 132, 1729
- Belczynski, K., Perna, R., Bulik, T., Kalogera, V., Ivanova, N., & Lamb, D. Q. 2006, *ApJ*, 648, 1110
- Berger, E. 2007, *ApJ*, 670, 1254
- Berger, E. 2010, *ApJ*, 722, 1946
- Berger, E., Cenko, S. B., Fox, D. B., & Cucchiara, A. 2009, *ApJ*, 704, 877
- Berger, E., et al. 2007, *ApJ*, 664, 1000
- Berger, E., Kulkarni, S. R., & Frail, D. A. 2003, *ApJ*, 590, 379
- Berger, E., et al. 2005, *Nature*, 438, 988
- Birkel, R., Aloy, M. A., Janka, H.-T., & Müller, E. 2007, *A&A*, 463, 51
- Blandford, R. D., & Znajek, R. L. 1977, *MNRAS*, 179, 433
- Bloom, J. S., Frail, D. A., & Kulkarni, S. R. 2003, *ApJ*, 594, 674
- Bloom, J. S., Kulkarni, S. R., & Djorgovski, S. G. 2002, *AJ*, 123, 1111
- Bloom, J. S., Sigurdsson, S., & Pols, O. R. 1999, *MNRAS*, 305, 763
- Burrows, D. N., et al. 2006, *ApJ*, 653, 468
- Campana, S., et al. 2011, *ArXiv e-prints*
- Cardelli, J. A., Clayton, G. C., & Mathis, J. S. 1989, *ApJ*, 345, 245
- Cenko, S. B., et al. 2011, *ApJ*, 732, 29
- Cenko, S. B., et al. 2010, *ApJ*, 711, 641
- Chandra, P., & Frail, D. A. 2011, *Bulletin of the Astronomical Society of India*, 39, 451
- Church, R. P., Levan, A. J., Davies, M. B., & Tanvir, N. 2011, *MNRAS*, 413, 2004
- Coward, D., et al. 2012, *ArXiv e-prints*
- Dai, Z. G., & Cheng, K. S. 2001, *ApJ*, 558, L109
- Darbhha, S., Metzger, B. D., Quataert, E., Kasen, D., Nugent, P., & Thomas, R. 2010, *MNRAS*, 409, 846
- De Pasquale, M., et al. 2010, *ApJ*, 709, L146
- Eichler, D., Livio, M., Piran, T., & Schramm, D. N. 1989, *Nature*, 340, 126
- Evans, P. A., et al. 2009, *MNRAS*, 397, 1177
- Evans, P. A., et al. 2007, *A&A*, 469, 379
- Filgas, R., et al. 2011, *A&A*, 526, A113
- Fong, W., et al. 2011, *ApJ*, 730, 26
- Fong, W., Berger, E., & Fox, D. B. 2010, *ApJ*, 708, 9
- Fox, D. B., et al. 2005, *Nature*, 437, 845
- Frail, D. A., et al. 2001, *ApJ*, 562, L55
- Friedman, A. S., & Bloom, J. S. 2005, *ApJ*, 627, 1
- Fryer, C. L., Woosley, S. E., & Hartmann, D. H. 1999, *ApJ*, 526, 152
- Galama, T. J., & Wijers, R. A. M. J. 2001, *ApJ*, 549, L209
- Gehrels, N., et al. 2004, *ApJ*, 611, 1005
- Ghirlanda, G., Ghisellini, G., & Lazzati, D. 2004, *ApJ*, 616, 331
- Goldstein, A., et al. 2011, *ArXiv e-prints*
- Granot, J., & Sari, R. 2002, *ApJ*, 568, 820
- Greisen, E. W. 2003, *Information Handling in Astronomy - Historical Vistas*, 285, 109
- Grupe, D., Burrows, D. N., Patel, S. K., Kouveliotou, C., Zhang, B., Mészáros, P., Wijers, R. A. M., & Gehrels, N. 2006, *ApJ*, 653, 462
- Hogg, D. W., Pahre, M. A., McCarthy, J. K., Cohen, J. G., Blandford, R., Smail, I., & Soifer, B. T. 1997, *MNRAS*, 288, 404
- Jakobsson, P., Hjorth, J., Fynbo, J. P. U., Watson, D., Pedersen, K., Björnsson, G., & Gorosabel, J. 2004, *ApJ*, 617, L21
- Jaroszynski, M. 1993, *AcA*, 43, 183
- Kalberla, P. M. W., Burton, W. B., Hartmann, D., Arnal, E. M., Bajaja, E., Morras, R., & Pöppel, W. G. L. 2005, *A&A*, 440, 775
- Kalogera, V., et al. 2004, *ApJ*, 601, L179
- Kocevski, D., & Butler, N. 2008, *ApJ*, 680, 531
- Kocevski, D., et al. 2010, *MNRAS*, 404, 963
- Kouveliotou, C., Meegan, C. A., Fishman, G. J., Bhat, N. P., Briggs, M. S., Koshut, T. M., Paciesas, W. S., & Pendleton, G. N. 1993, *ApJ*, 413, L101
- Lee, W. H., & Ramirez-Ruiz, E. 2007, *New Journal of Physics*, 9, 17
- Levan, A. J., Wynn, G. A., Chapman, R., Davies, M. B., King, A. R., Priddey, R. S., & Tanvir, N. R. 2006, *MNRAS*, 368, L1
- Levesque, E. M., et al. 2010, *MNRAS*, 401, 963
- Liang, E.-W., Zhang, B.-B., & Zhang, B. 2007, *ApJ*, 670, 565
- Mangano, V., & Sakamoto, T. 2011, *GRB Coordinates Network*, 12468, 1
- Margutti, R., et al. 2010, *MNRAS*, 402, 46
- Margutti, R., et al. 2012, *ArXiv e-prints*
- Metzger, B. D., & Berger, E. 2012, *ApJ*, 746, 48
- Metzger, B. D., Quataert, E., & Thompson, T. A. 2008, *MNRAS*, 385, 1455
- Mochkovitch, R., Hernanz, M., Isern, J., & Martin, X. 1993, *Nature*, 361, 236
- Nakar, E., Gal-Yam, A., & Fox, D. B. 2006, *ApJ*, 650, 281
- Nakar, E., & Granot, J. 2007, *MNRAS*, 380, 1744
- Narayan, R., Paczynski, B., & Piran, T. 1992, *ApJ*, 395, L83
- Nicuesa Guelbenzu, A., et al. 2012, *A&A*, 538, L7
- Nicuesa Guelbenzu, A., et al. 2011, *A&A*, 531, L6
- Nousek, J. A., et al. 2006, *ApJ*, 642, 389
- Oates, S. R., & Sakamoto, T. 2011, *GRB Coordinates Network*, 12466, 1
- Osborne, J. P., Beardmore, A. P., Evans, P. A., & Goad, M. R. 2011, *GRB Coordinates Network*, 12463, 1
- Panaitescu, A. 2006, *MNRAS*, 367, L42
- Panaitescu, A., & Kumar, P. 2001, *ApJ*, 560, L49
- Perley, D. A., et al. 2009a, *AJ*, 138, 1690
- Perley, D. A., et al. 2009b, *ApJ*, 696, 1871
- Perley, R. A., Chandler, C. J., Butler, B. J., & Wrobel, J. M. 2011, *ApJ*, 739, L1
- Perna, R., & Belczynski, K. 2002, *ApJ*, 570, 252
- Poole, T. S., et al. 2008, *MNRAS*, 383, 627
- Popham, R., Woosley, S. E., & Fryer, C. 1999, *ApJ*, 518, 356
- Predehl, P., & Schmitt, J. H. M. M. 1995, *A&A*, 293, 889
- Qin, B., Wu, X.-P., Chu, M.-C., Fang, L.-Z., & Hu, J.-Y. 1998, *ApJ*, 494, L57
- Racusin, J. L., et al. 2009, *ApJ*, 698, 43
- Reddy, N. A., & Steidel, C. C. 2009, *ApJ*, 692, 778
- Rees, M. J., & Meszaros, P. 1998, *ApJ*, 496, L1
- Rezzolla, L., Giacomazzo, B., Baiotti, L., Granot, J., Kouveliotou, C., & Aloy, M. A. 2011, *ApJ*, 732, L6
- Rhoads, J. E. 1999, *ApJ*, 525, 737
- Rosswog, S. 2005, *Nuovo Cimento C Geophysics Space Physics C*, 28, 607
- Rosswog, S., Ramirez-Ruiz, E., & Davies, M. B. 2003, *MNRAS*, 345, 1077
- Ruffert, M., & Janka, H. 1999a, *Progress of Theoretical Physics Supplement*, 136, 287
- Ruffert, M., & Janka, H.-T. 1999b, *A&A*, 344, 573
- Sakamoto, T., et al. 2011a, *GRB Coordinates Network*, 12464, 1
- Sakamoto, T., Barthelmy, S. D., & Norris, J. 2011, *GRB Coordinates Network*, 12477, 1
- Sakamoto, T., et al. 2011b, *GRB Coordinates Network*, 12460, 1
- Salvaterra, R., Devecchi, B., Colpi, M., & D'Avanzo, P. 2010, *MNRAS*, 406, 1248
- Sari, R., & Mészáros, P. 2000, *ApJ*, 535, L33
- Sari, R., Piran, T., & Halpern, J. P. 1999, *ApJ*, 519, L17
- Sari, R., Piran, T., & Narayan, R. 1998, *ApJ*, 497, L17
- Schlaflly, E. F., & Finkbeiner, D. P. 2011, *ApJ*, 737, 103
- Schlegel, D. J., Finkbeiner, D. P., & Davis, M. 1998, *ApJ*, 500, 525
- Soderberg, A. M., et al. 2006, *ApJ*, 650, 261
- Stratta, G., et al. 2007, *A&A*, 474, 827
- van der Horst, A. J., Kouveliotou, C., Gehrels, N., Rol, E., Wijers, R. A. M. J., Cannizzo, J. K., Racusin, J., & Burrows, D. N. 2009, *ApJ*, 699, 1087
- Wakker, B. P., Lockman, F. J., & Brown, J. M. 2011, *ApJ*, 728, 159
- Watson, D. 2011, *A&A*, 533, A16
- Watson, D., Hjorth, J., Jakobsson, P., Xu, D., Fynbo, J. P. U., Sollerman, J., Thöne, C. C., & Pedersen, K. 2006, *A&A*, 454, L123
- Willmer, C. N. A., et al. 2006, *ApJ*, 647, 853
- Xin, L.-P., et al. 2011, *MNRAS*, 410, 27
- Zhang, B., Fan, Y. Z., Dyks, J., Kobayashi, S., Mészáros, P., Burrows, D. N., Nousek, J. A., & Gehrels, N. 2006, *ApJ*, 642, 354
- Zhang, B., & Mészáros, P. 2002, *ApJ*, 566, 712

TABLE 1
GRB 111020A X-RAY SPECTRAL FIT PARAMETERS

| Telescope | Detector | δt (ks) | $N_{\text{H,int}}^{ab}$ (10^{22} cm^{-2}) | Γ^{ab} | C-stat $_{\nu}$ /d.o.f. |
|-------------------|-------------|--------------------|--|---------------------|-------------------------|
| <i>Swift</i> | XRT | 0.08–60 | 1.0 ± 0.3 | 2.2 ± 0.5 | 0.86/188 |
| XMM | EPIC-PN | 61.4–76.8 | $0.65^{+0.21}_{-0.23}$ | 2.0 ± 0.4 | 1.0/256 |
| <i>Chandra</i> | ACIS-S | 250.5–268.5 | $0.4^{+2.3}_{-0.4}$ | $1.1^{+2.7}_{-0.8}$ | 0.32/661 |
| <i>Swift</i> +XMM | XRT+EPIC-PN | see above | $0.75^{+0.20}_{-0.18}$ | 2.0 ± 0.3 | 0.94/446 |

NOTE. — ^a These values assume a Galactic column density of $N_{\text{H,gal}} = 6.9 \times 10^{20} \text{ cm}^{-2}$ (Kalberla et al. 2005), using an XSPEC model of $tbabs \times ztbabs \times pow$ at $z=0$.

^b Uncertainties correspond to a 90% confidence level.

TABLE 2
GRB 111020A X-RAY OBSERVATIONS

| δt (s) | Time Bin Duration (s) | Unabs. Flux (0.3–10 keV) (erg cm ⁻² s ⁻¹) |
|-----------------------|--------------------------|---|
| <i>Swift/XRT</i> | | |
| 6.18×10^{1a} | 7.44×10^0 | $(2.38 \pm 0.79) \times 10^{-10}$ |
| 1.35×10^2 | 4.64×10^1 | $(3.80 \pm 1.03) \times 10^{-11}$ |
| 2.66×10^2 | 1.71×10^2 | $(1.64 \pm 0.42) \times 10^{-11}$ |
| 4.15×10^2 | 1.26×10^2 | $(2.43 \pm 0.64) \times 10^{-11}$ |
| 5.96×10^2 | 2.36×10^2 | $(1.03 \pm 0.26) \times 10^{-11}$ |
| 7.97×10^2 | 1.66×10^2 | $(1.83 \pm 0.49) \times 10^{-11}$ |
| 1.14×10^3 | 5.20×10^2 | $(8.85 \pm 1.72) \times 10^{-12}$ |
| 5.94×10^3 | 2.46×10^3 | $(1.65 \pm 0.33) \times 10^{-12}$ |
| 1.17×10^4 | 2.46×10^3 | $(1.07 \pm 0.27) \times 10^{-12}$ |
| 1.94×10^4 | 6.38×10^3 | $(9.19 \pm 2.28) \times 10^{-13}$ |
| 2.58×10^4 | 6.28×10^3 | $(1.19 \pm 0.32) \times 10^{-12}$ |
| 3.19×10^4 | 5.90×10^3 | $(1.05 \pm 0.27) \times 10^{-12}$ |
| 4.29×10^4 | 1.61×10^4 | $(8.36 \pm 2.41) \times 10^{-13}$ |
| 1.26×10^5 | 1.51×10^5 | $(1.63 \pm 0.55) \times 10^{-13}$ |
| 3.09×10^5 | 2.14×10^5 | $(1.11 \pm 0.42) \times 10^{-13}$ |
| <i>XMM/EPIC-PN</i> | | |
| 6.91×10^4 | 1.35×10^4 | $(2.66 \pm 0.19) \times 10^{-13}$ |
| <i>Chandra/ACIS-S</i> | | |
| 2.61×10^5 | 1.98×10^4 | $(5.96 \pm 0.89) \times 10^{-14}$ |
| 8.84×10^5 | 1.98×10^4 | $< 8.95 \times 10^{-15}$ |

NOTE. — Upper limits are 3σ .

^a These points were excluded from the broken power law fit.

TABLE 3
GRB 111020A OPTICAL PHOTOMETRY

| Date (UT) | Δt (d) | Telescope | Instrument | Filter | Exposures (s) | θ_{FWHM} (arcsec) | Afterglow ^{ab} (AB mag) | F_{ν}^{ab} (μJy) | G1 ^a (AB mag) | G2 ^a (AB mag) | G3 ^a (AB mag) |
|--------------------------|-------------------|---------------|------------|----------|------------------|------------------------------------|-------------------------------------|--------------------------------------|-----------------------------|-----------------------------|-----------------------------|
| 2011 October 21.01 | 0.74 | Magellan/Clay | LDSS3 | <i>r</i> | 3×360 | 0.62 | > 23.4 | < 1.56 | > 23.4 | 21.12 ± 0.09 | > 23.4 |
| 2011 October 21.01 | 0.74 | Gemini-S | GMOS | <i>i</i> | 9×180 | 0.74 | > 24.4 | < 0.63 | | | |
| 2011 October 22.01 | 1.74 | Gemini-S | GMOS | <i>i</i> | 11×180 | 0.67 | | | | | |
| 2011 October 21.01+22.01 | | Gemini-S | GMOS | <i>i</i> | 20×180 | 0.72 | | | 23.89 ± 0.17 | 21.91 ± 0.05 | 24.27 ± 0.16 |

NOTE. — ^a These values have been corrected for Galactic extinction A_{λ} (Schlafly & Finkbeiner 2011).

^b Limits are 3σ .

TABLE 4
PHYSICAL PARAMETERS OF GRB 111020A

| Parameter | Case I [$z = 0.5, \epsilon_e = \epsilon_B = 1/3$] | Case II [$z = 1.5, \epsilon_e = \epsilon_B = 0.1$] |
|-------------------------|---|--|
| t_j | 2.0 ± 0.5 days ^a | 2.0 ± 0.5 days ^a |
| $E_{\gamma,\text{iso}}$ | 2.1×10^{50} erg | 1.9×10^{51} erg |
| $E_{K,\text{iso}}$ | 3.7×10^{50} erg | 1.2×10^{52} erg |
| n_0 | $0.01 - 0.06$ cm ⁻³ | 0.008 cm ⁻³ |
| θ_j | $7 - 8^\circ$ | 3° |
| f_b | $0.007 - 0.01$ | 0.001 |
| E_γ | 2×10^{48} erg | 3×10^{48} erg |
| E_K | $(3 - 4) \times 10^{48}$ erg | 2×10^{49} erg |
| E_{tot} | $(5 - 6) \times 10^{48}$ erg | 2×10^{49} erg |
| η_γ | $0.3 - 0.4$ | 0.15 |

NOTE. — ^a Uncertainties correspond to a 1σ confidence level.

TABLE 5
INTRINSIC X-RAY COLUMN DENSITY OF
HYDROGEN, $N_{\text{H,int}}$ FOR *Swift* SHORT GRBS

| GRB | z | $N_{\text{H,int}}$ (10^{21} cm^{-2}) | σ above zero |
|---------|-------|---|---------------------|
| 050724 | 0.258 | $3.20^{+0.97}_{-0.86}$ | 5.7 |
| 051210 | ... | < 0.54 | |
| 051221A | 0.547 | $1.92^{+0.73}_{-0.68}$ | 4.5 |
| 060313 | ... | $0.45^{+0.56}_{-0.33}$ | 2.1 |
| 060801 | 1.131 | $3.02^{+2.22}_{-1.88}$ | 2.4 |
| 061006 | 0.438 | < 2.04 | |
| 061201 | ... | $0.94^{+0.60}_{-0.53}$ | 2.7 |
| 070714B | 0.923 | $3.89^{+1.87}_{-1.61}$ | 4.2 |
| 070724A | 0.457 | < 1.89 | |
| 071227 | 0.383 | $2.84^{+0.72}_{-0.65}$ | 6.8 |
| 080123 | ... | $1.12^{+0.58}_{-0.26}$ | 6.8 |
| 080905A | 0.122 | $2.04^{+1.58}_{-1.33}$ | 2.3 |
| 090510 | 0.903 | < 0.80 | |
| 090515 | ... | $0.56^{+0.30}_{-0.27}$ | 3.2 |
| 090607 | ... | < 0.79 | |
| 091109B | ... | < 1.58 | |
| 100117A | 0.915 | $4.10^{+3.41}_{-2.71}$ | 2.2 |
| 100702A | ... | $4.37^{+3.67}_{-3.05}$ | 2.1 |
| 101219A | 0.718 | $6.61^{+3.73}_{-2.82}$ | 3.3 |
| 110112A | ... | < 0.92 | |
| 111020A | ... | $7.50^{+2.0}_{-1.8}$ | 6.5 |
| 111117A | ... | $1.84^{+1.28}_{-1.05}$ | 2.6 |
| 111121A | ... | $2.41^{+0.82}_{-0.74}$ | 5.1 |

NOTE. — Errors and upper limits quoted correspond to a 90% confidence level; $z = 0$ is assumed when the redshift is not known.

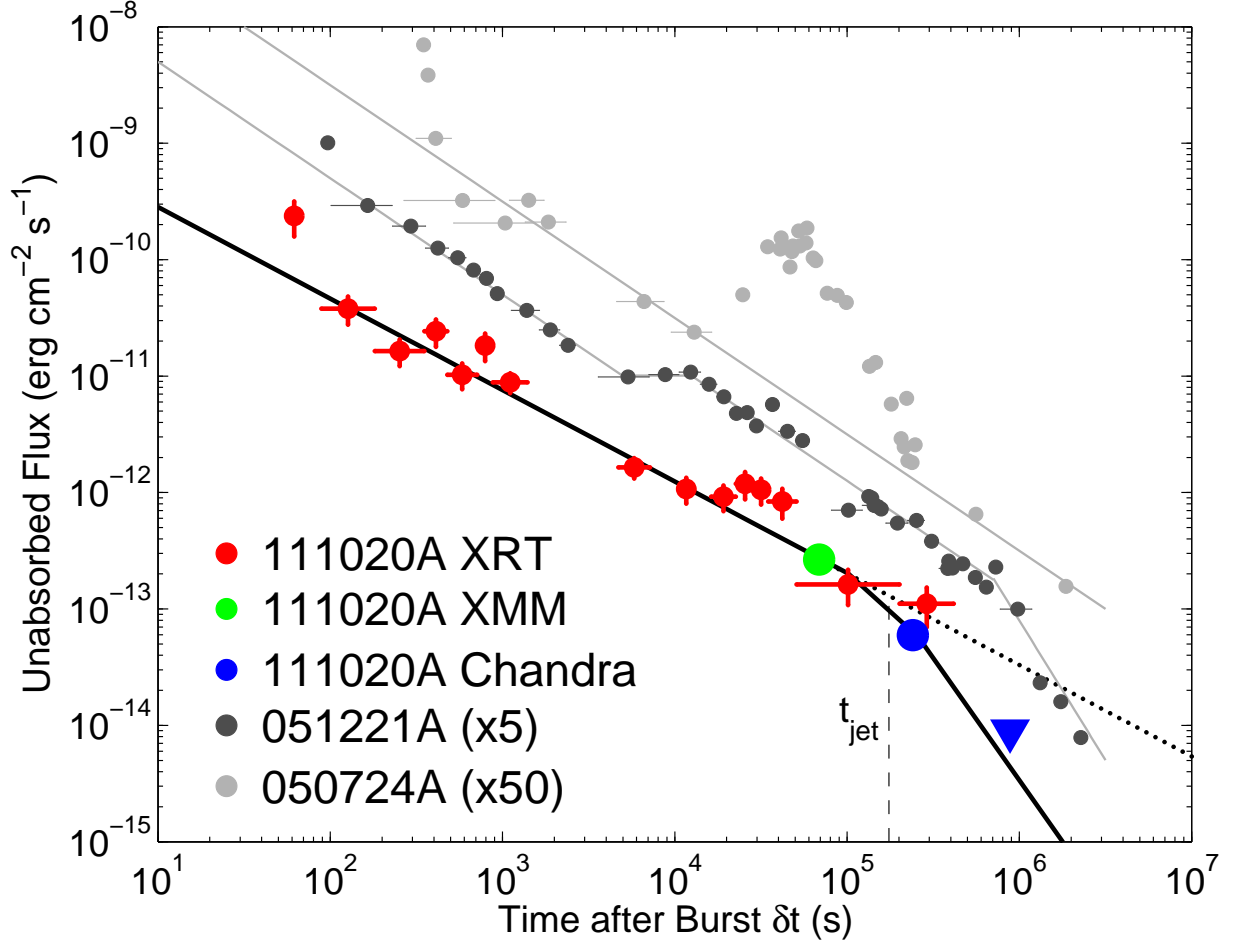


FIG. 1.— Unabsorbed X-ray flux light curve for GRB 111020A from *Swift*-XRT (red), XMM (green), and *Chandra* (blue). Flux errors are 1σ . The *Chandra* 3σ upper limit is denoted by the blue triangle. The best-fit broken power law model (black solid line) for GRB 111020A is characterized by $\alpha_1 = -0.78$, $\alpha_2 = -2.1$, and $t_j = 2.0$ days. A single power law model with $\alpha = -0.78$ (black dotted) violates the *Chandra* upper limit. Also plotted are X-ray light curves for short GRBs 051221A (dark grey circles; Soderberg et al. 2006; Burrows et al. 2006) and 050724 (light grey circles; Grupe et al. 2006). The data for GRBs 051221A and 050724 have been scaled for clarity. Grey lines trace the afterglow evolution with a break for GRB 051221A at ≈ 5 days and no break for GRB 050724A to ≈ 22 days.

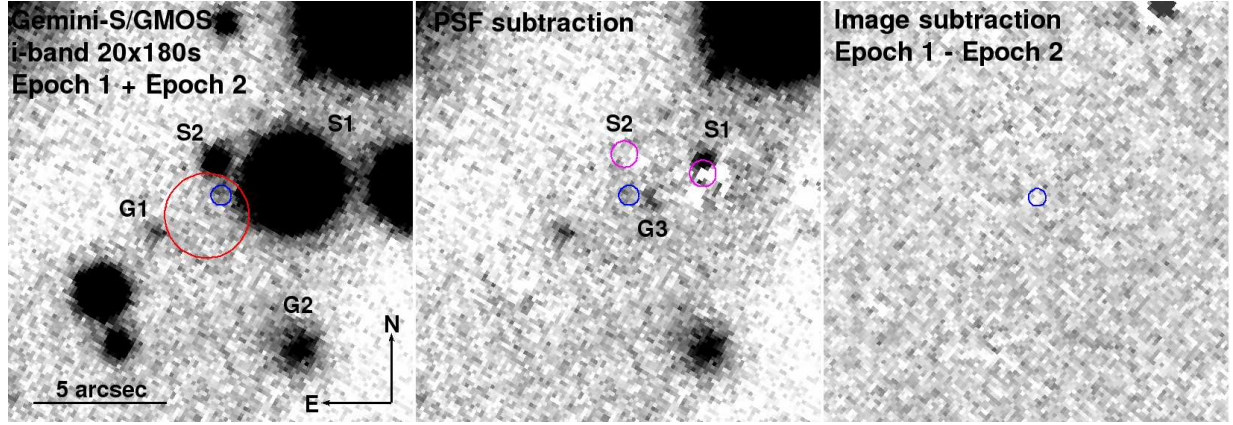


FIG. 2.— Optical *i*-band observations obtained with GMOS on Gemini-South. *Left*: Combined stack of two nights of GMOS *i*-band data. Stars S1 and S2 are labeled, as well as galaxies G1 and G2. X-ray positions of GRB 111020A are denoted by the circles (red: *Swift*-XRT, $1.6''$ radius, 90% containment; blue: *Chandra*, $0.33''$ radius, 90% confidence). *Center*: PSF-subtracted image with the centroids of S1 and S2 (magenta circles). The subtraction reveals a third source, G3, with $i \approx 24.3$ mag. *Right*: Digital image subtraction of the two epochs obtained at 17.7 hours and 1.7 days, respectively, reveals no residuals in or around the *Chandra* position.

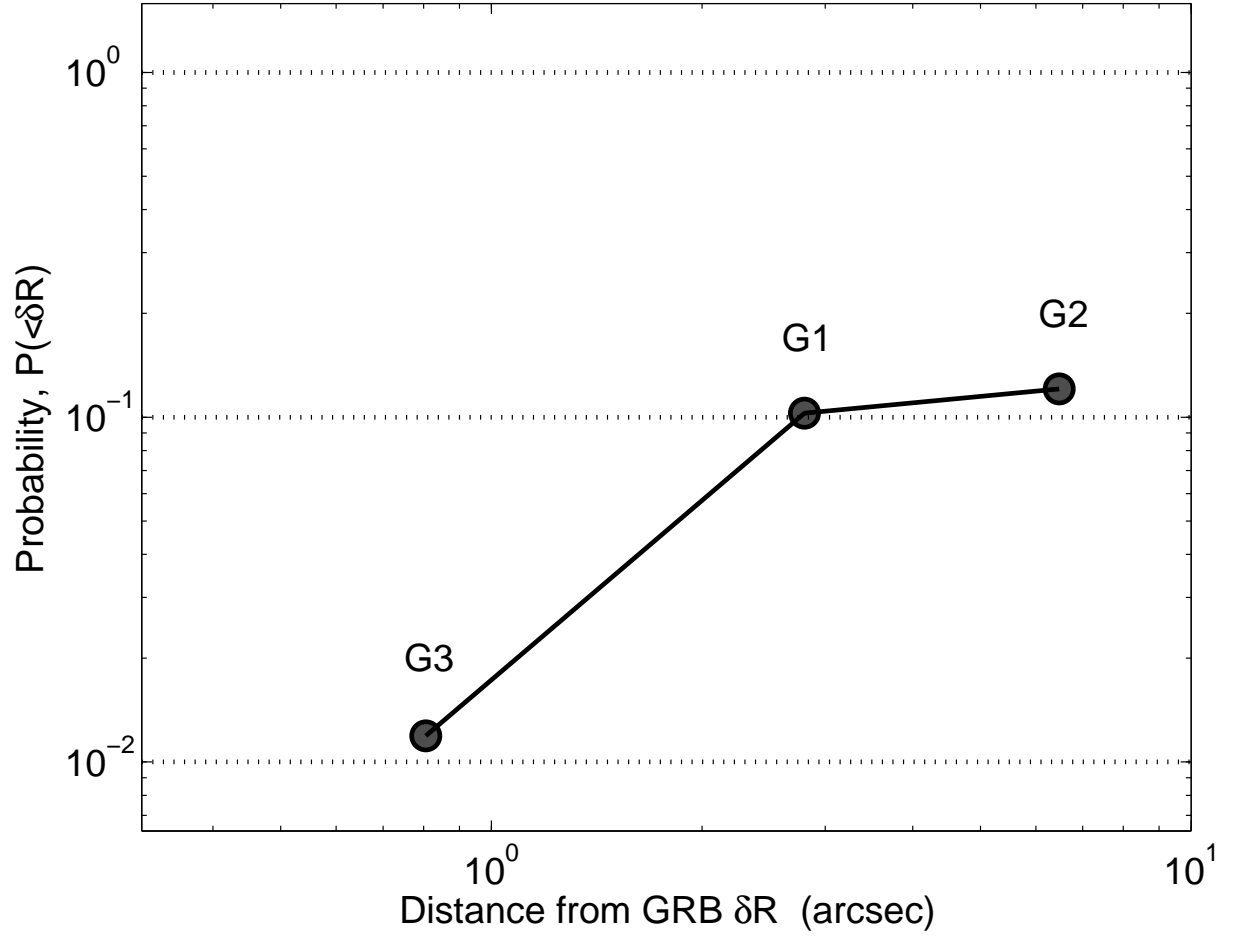


FIG. 3.— Probability of chance coincidence, $P(<\delta R)$, as a function of angular distance from the center of the *Chandra* afterglow position for the three host galaxy candidates of GRB 111020A. The galaxy G3 has the lowest probability of chance coincidence $P(<\delta R) = 0.01$, and is therefore the most probable host of GRB 111020A.

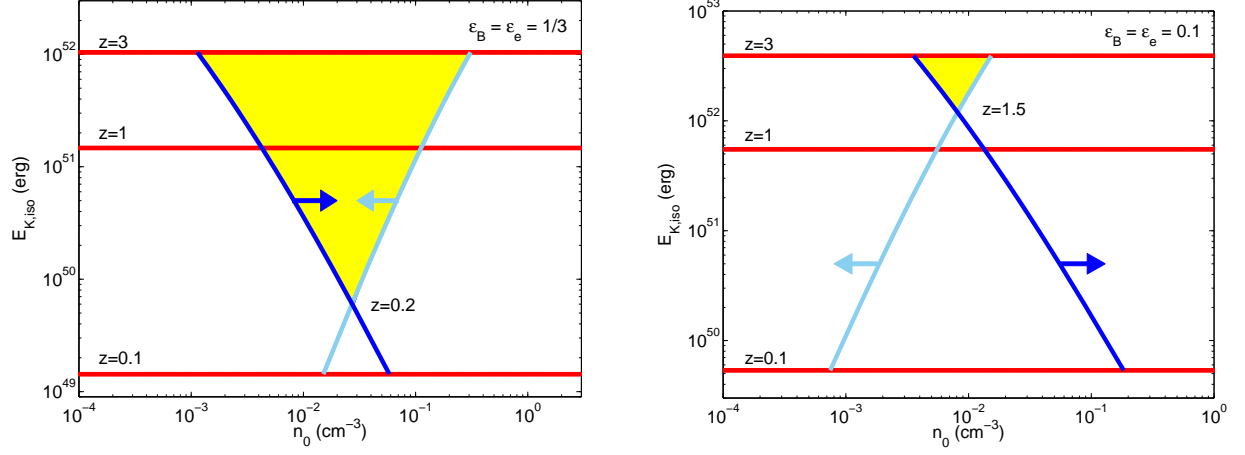


FIG. 4.— Isotropic-equivalent kinetic energy and circumburst density parameter space for GRB 111020A assuming $\epsilon_e = \epsilon_B = 1/3$ (left) and $\epsilon_e = \epsilon_B = 0.1$ (right). The lower limit on the density (dark blue) is set by the condition that $\nu_c < \nu_X$ (Equation 6) while the upper limit (light blue) is set by radio observations (Equation 5). Also plotted are the values for $E_{K,iso}$ at $z = 0.1, 1$ and 3 (red). The allowable parameter space set by these constraints is filled in yellow.

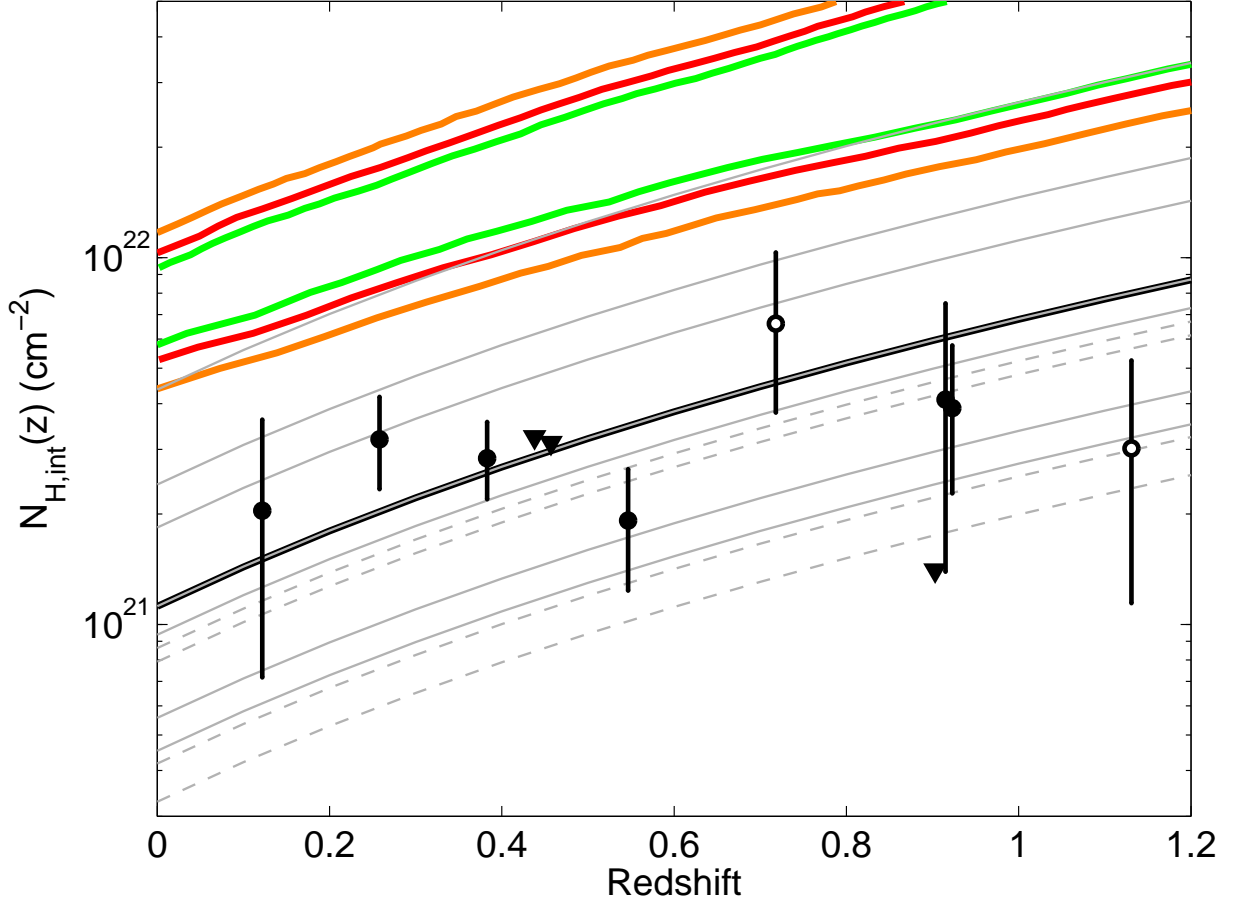


FIG. 5.— Excess neutral hydrogen column density, $N_{\text{H,int}}$, versus redshift for GRB 111020A (1, 2 and 3σ intervals denoted by green, red and orange lines) along with 6 *Swift* short GRBs with measured redshifts and optical afterglows (black filled circles) and 2 (GRBs 060801 and 101219A) with only X-ray afterglows (open circles). Also plotted are 11 short GRBs without secure redshifts (grey lines), 4 of which have only upper limits on $N_{\text{H,int}}$ (grey dashed). For GRBs without redshifts, the $N_{\text{H,int}}$ value at $z = 0$ is scaled by $(1+z)^{2.6}$ (Galama & Wijers 2001). Errors and upper limits are at the 90% confidence level. The weighted mean for all short GRBs (black line) over the redshift interval $z = 0 - 1.2$ is also shown. GRB 111020A has the highest $N_{\text{H,int}}$ of a short GRB to date and is well above the mean for short GRBs.

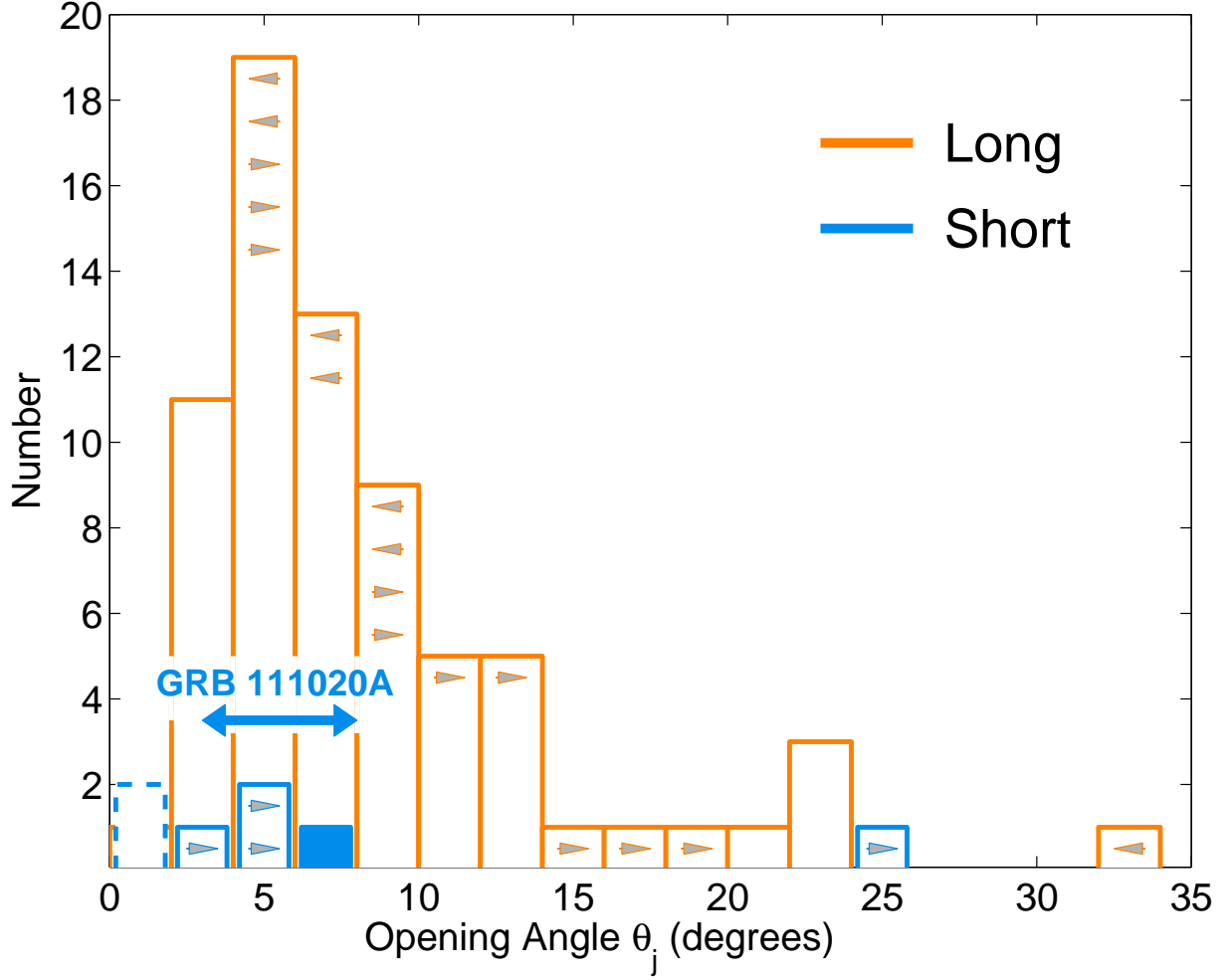


FIG. 6.— Distribution of opening angles for long (orange) and short (blue) GRBs. Arrows represent upper and lower limits. The long GRB population includes pre-*Swift* (Frail et al. 2001; Berger et al. 2003; Bloom et al. 2003; Ghirlanda et al. 2004; Friedman & Bloom 2005), *Swift* (Racusin et al. 2009; Filgas et al. 2011), and *Fermi* (Cenko et al. 2010; Goldstein et al. 2011; Cenko et al. 2011) bursts. The opening angle for GRB 111020A ranges from $\sim 3-8^\circ$ (depending on the redshift), while GRB 051221A has $\theta_j \approx 7^\circ$ (Soderberg et al. 2006; Burrows et al. 2006). Tentative jet breaks (blue dashed) for GRBs 061201 (Stratta et al. 2007) and 090510 (De Pasquale et al. 2010; Nicuesa Guelbenzu et al. 2012) are at $\sim 1^\circ$. Short GRB lower limits are from the non-detection of jet breaks in *Swift*/XRT data (this work, revised from Coward et al. 2012) and *Chandra* data for GRB 050724A (Berger et al. 2005; Grupe et al. 2006).